



THERMODYNAMIC SPECTRUM OF SOLAR FLARES BASED ON *SDO*/EVE OBSERVATIONS: TECHNIQUES AND FIRST RESULTS

YUMING WANG^{1,2}, ZHENJUN ZHOU¹, JIE ZHANG³, KAI LIU¹, RUI LIU^{1,4}, CHENGLONG SHEN^{1,2}, AND PHILLIP C. CHAMBERLIN⁵

¹CAS Key Laboratory of Geospace Environment, Department of Geophysics and Planetary Sciences, University of Science and Technology of China, Hefei, Anhui 230026, China; ymwang@ustc.edu.cn

²Synergetic Innovation Center of Quantum Information & Quantum Physics, University of Science and Technology of China, Hefei, Anhui 230026, China

³School of Physics, Astronomy and Computational Sciences, George Mason University, 4400 University Drive, MSN 6A2, Fairfax, VA 22030, USA

⁴Collaborative Innovation Center of Astronautical Science and Technology, Hefei 230026, China

⁵Solar Physics Laboratory, Heliophysics Division, NASA Goddard Space Flight Center, Greenbelt, MD 20771, USA

Received 2015 September 1; accepted 2016 January 19; published 2016 March 9

ABSTRACT

The *Solar Dynamics Observatory* (*SDO*)/EUV Variability Experiment (EVE) provides rich information on the thermodynamic processes of solar activities, particularly on solar flares. Here, we develop a method to construct thermodynamic spectrum (TDS) charts based on the EVE spectral lines. This tool could potentially be useful for extreme ultraviolet (EUV) astronomy to learn about the eruptive activities on distant astronomical objects. Through several cases, we illustrate what we can learn from the TDS charts. Furthermore, we apply the TDS method to 74 flares equal to or greater than the M5.0 class, and reach the following statistical results. First, EUV peaks are always behind the soft X-ray (SXR) peaks and stronger flares tend to have faster cooling rates. There is a power-law correlation between the peak delay times and the cooling rates, suggesting a coherent cooling process of flares from SXR to EUV emissions. Second, there are two distinct temperature drift patterns, called Type I and Type II. For Type I flares, the enhanced emission drifts from high to low temperature like a quadrilateral, whereas for Type II flares the drift pattern looks like a triangle. Statistical analysis suggests that Type II flares are more impulsive than Type I flares. Third, for late-phase flares, the peak intensity ratio of the late phase to the main phase is roughly correlated with the flare class, and the flares with a strong late phase are all confined. We believe that the re-deposition of the energy carried by a flux rope, which unsuccessfully erupts out, into thermal emissions is responsible for the strong late phase found in a confined flare. Furthermore, we show the signatures of the flare thermodynamic process in the chromosphere and transition region in the TDS charts. These results provide new clues to advance our understanding of the thermodynamic processes of solar flares and associated solar eruptions, e.g., coronal mass ejections.

Key words: Sun: corona – Sun: coronal mass ejections (CMEs) – Sun: flares – Sun: UV radiation

1. INTRODUCTION

As some of the most catastrophic events on the Sun, solar flares directly impact the environment of interplanetary space and the Earth's atmosphere. During a flare process, free magnetic energy is converted into electromagnetic radiation, energetic particles, heated plasma, waves, etc. (e.g., Hudson 2011). The radiation occupies the majority of the flare energy (Emslie et al. 2012). Extreme ultraviolet (EUV) wavelengths, from about 10 to 120 nm, are a main window into solar activities (Fröhlich & Lean 2004). Although it occupies a small fraction of solar total irradiance, the majority of the Sun's variability appears in the EUV output (e.g., Woods et al. 2006; Moore et al. 2014).

The history of solar EUV observations could be traced back to sounding rocket and satellite experiments (Friedman 1963). After that, many space missions, e.g., the *Solar and Heliospheric Observatory* (*SOHO*), the *Transition Region and Coronal Explorer* (*TRACE*), the *Ramaty High Energy Solar Spectroscopic Imager* (*RHESSI*), *Hinode*, the *Solar Terrestrial Relations Observatory* (*STEREO*), and the *Solar Dynamics Observatory* (*SDO*), made significant observational achievements using their imaging spectrographs with high spatial resolution and EUV broadbands. With the exception of the EUV observations for the Sun, there are also many EUV observations for stellar sources, such as those by the *Extreme*

Ultraviolet Explorer (*EUVE*) satellite, which acquired data in the wavelength from about 7 to 76 nm (Craig et al. 1997).

One of the most recent space-borne instruments for solar EUV observations is the EUV Variability Experiment (EVE; - Woods et al. 2012) on board the *SDO* (Pesnell et al. 2012), which has an unprecedented high cadence of 10 s, subtle spectral resolution of 0.1 nm, and breakthrough wavelength range from 5 to 105 nm. Due to its excellent performance, some new features of the solar irradiance are revealed (e.g., Woods et al. 2011; Chamberlin et al. 2012; Milligan et al. 2012a, 2012b; Liu et al. 2013, 2015; Ryan et al. 2013; Warren et al. 2013), particularly on the aspect of solar flares. For example, a new phase of flares, called late phase, was found after the flare's main phase at warm coronal lines (Woods et al. 2011). A joint analysis with the imaging data from the *SDO*/Atmospheric Imaging Assembly (AIA; Lemen et al. 2012) suggested that further enhancement of emissions at warm coronal lines during the late phase is associated with the heating of separate coronal loops immediately next to the main flare loops (e.g., Woods et al. 2011; Liu et al. 2013). Chamberlin et al. (2012) and Ryan et al. (2013) studied the thermal evolution and radiative output of flares. Warren et al. (2013) argued that the isothermal postulate seems unreasonable for the thermal structure of a flare through comparing EVE spectra with calculations based on parameters derived from the *GOES* soft X-ray (SXR) fluxes.

Table 1
Emission Lines Provided by MEGS-A EVL Product*

No.	Ions	λ_{\min} (nm)	λ_{\max} (nm)	λ_{cen} (nm)	$\log(T)$ log (K)	$\sigma_{T\pm}$ ($\times 10^{-7} \text{ W m}^{-2}$)	$\sigma_{G\pm}$ ($\times 10^{-9} \text{ W m}^{-2} \text{ s}^{-1}$)
1	Fe xx*	13.23	13.32	13.29	6.97	+9.3/−0.2	+2.3/−1.6
2	Fe xviii*	9.33	9.43	9.39	6.81	+5.5/−1.7	+0.6/−0.4
3	Fe xvi*	33.47	33.61	33.54	6.43	+28.2/−21.8	+1.9/−1.7
4	Fe xvi	36.02	36.20	36.08	6.43
5	Fe xv*	28.30	28.50	28.42	6.30	+30.1/−26.8	+1.3/−1.2
6	Fe xiv	21.07	21.20	21.13	6.27
7	Fe xiii	20.14	20.32	20.20	6.19
8	Fe xii*	19.43	19.61	19.51	6.13	+17.9/−10.1	+1.8/−1.7
9	Fe xi*	17.96	18.15	18.04	6.07	+11.2/−12.2	+1.2/−1.1
10	Fe x	17.63	17.83	17.72	5.99
11	Mg ix	36.71	36.89	36.81	5.99
12	Fe ix*	17.02	17.24	17.11	5.81	+14.4/−14.5	+1.5/−1.5
13	Fe viii*	13.04	13.17	13.12	5.57	+0.5/−0.5	+0.1/−0.1
14	He ii	25.55	25.68	25.63	4.75
15	He ii	30.25	30.50	30.38	4.70

Note.

* Columns 3–5 give the wavelength range and peak wavelength of each spectral line, Column 6 lists the corresponding formation temperature, and the last two columns give the deviations of the variabilities and gradients of final selected spectral lines (see Section 2.2 for more details).

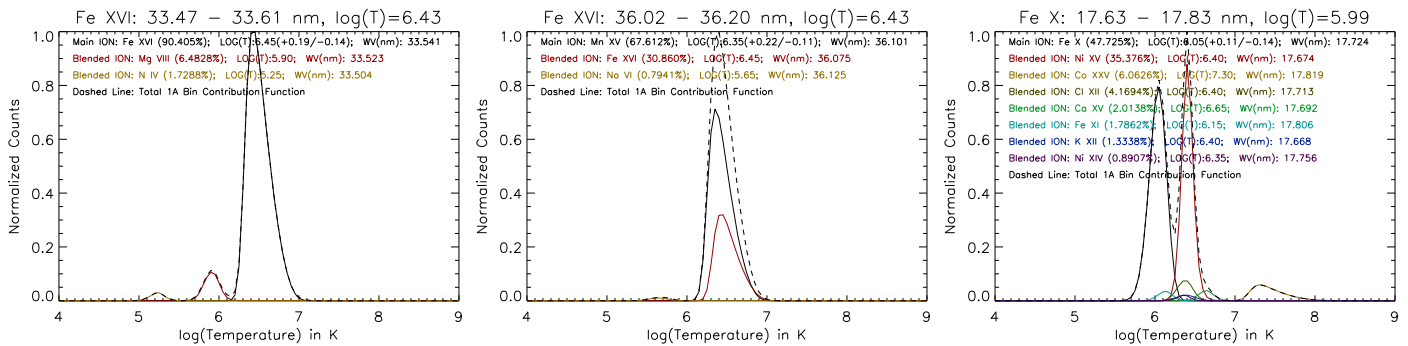


Figure 1. Temperature response curves derived based on the CHIANTI atomic database. The left and middle panels are for the lines Fe xvi 33.54 nm and Fe xvi 36.08 nm, which have the same formation temperature as indicated in the EVE level 2 data. The CHIANTI calculation suggests that Fe xvi is the main ion for the emission within the wavelength band of 33.47–33.61 nm, but is a minor ion within the wavelength band of 36.02–36.20 nm. The right panel shows the temperature response curves for the wavelength band of 17.63–17.83 nm, in which Fe x 17.72 nm is the main emission but is significantly blended by Ni xv 17.67 nm. In each panel, the percentages given in the parentheses are the ratios of the contribution of the ion to the total emission within the given wavelength range, and the temperature uncertainty of the main ion is read from the FWHM of its emission peak.

Each emission line in EUV is produced by a particular element in a particular ionization level that corresponds to a formation temperature. Thus, EVE data, with its high resolution in both wavelength and time, provide us a unique opportunity to study the thermal dynamics of solar activities, though it does not have spatial resolution. So far, most studies of EVE data investigated the temporal profile of each individual spectral line, which is not efficient and may miss some interesting features. In this paper, we develop a method to construct the EVE thermodynamic spectrum (TDS) chart, a two-dimensional (2D) image of emission line intensity or other relevant quantities against temperature (along the Y-axis) and time (along the X-axis). This is similar to the dynamic spectrum of radio emission, which is a 2D image of radio emission intensity against frequency and time. As will be seen below, the charts could provide a global view of the thermal process of solar activities, particularly of solar flares, reflected in the EUV wavelengths. The description of the data and method are given in the next section.

2. DATA AND METHOD

2.1. Selection of Emission Lines

The EVE instrument has three subsystems, among which MEGS (Multiple EUV Grating Spectrograph) measures the spectral irradiance from 5 to 105 nm, with 0.1 nm spectral resolution and a 10 s cadence (Woods et al. 2012). MEGS has four channels: MEGS-A, MEGS-B, MEGS-SAM, and MEGS-P. Our study is based on data from MEGS-A and MEGS-B, which were designed for the wavelength ranges 5–37 nm and 35–105 nm, respectively. MEGS provides several level 2 data products, including the “line” (EVL) product and the “spectra” (EVS) product. The EVL product consists of 30 emission lines; half of them are extracted from the MEGS-A EVS data and the other half are from the MEGS-B EVS data (refer to the readme file at EVE’s official website: <http://lasp.colorado.edu/home/eve/science/instrument/>). MEGS-A has full coverage in time (except for the eclipse time for *SDO*), whereas MEGS-B does not operate full time and was typically opened for about five minutes

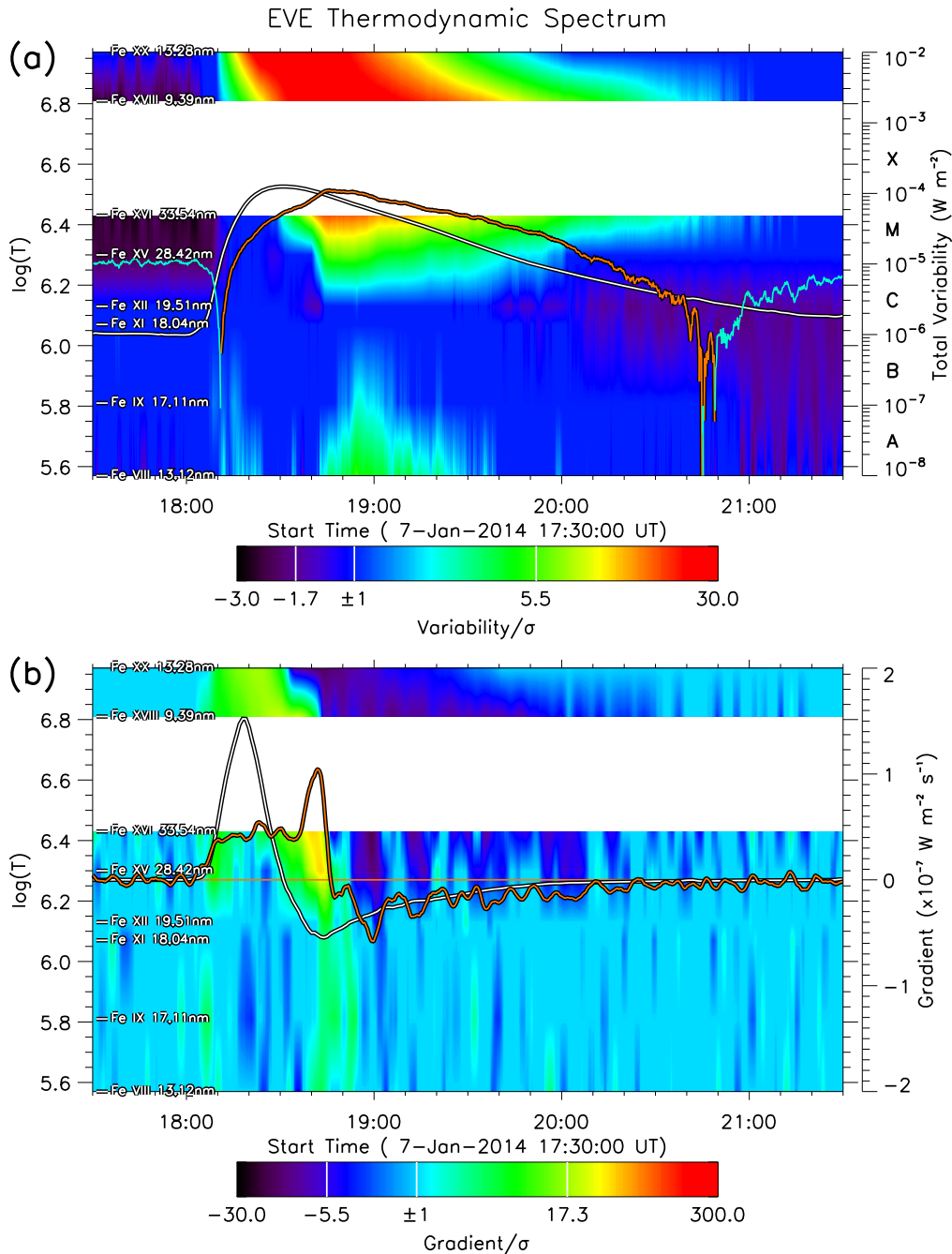


Figure 2. EVE TDS charts. Panel (a) shows the variability and panel (b) shows the gradient. See Section 2.2 for the definitions of variability and gradient. The eight emission lines used in the charts are indicated on the left. The orange line in panel (a) is the total variability of these lines with the y-axis on the right, and the orange line in panel (b) is the gradient of the total variability. The white lines are derived from *GOES* SXR for the wavelength bands of 1–8 Å.

every hour. Although the MEGS-A channel was lost on 2014 May 26, five years of data have been acquired and thousands of flares have been observed, to which the TDS analysis can be applied. We first use the data from MEGS-A only to demonstrate how to construct the TDS charts in this section, and present the case and statistical studies on solar flares based on the TDS in Sections 3–4. Then we show the extended TDS charts constructed by combining both MEGS-A and MEGS-B data in Section 5, as the sporadic MEGS-B data also recorded hundreds of flares.

Table 1 lists the extracted emission lines provided by the MEGS-A EVL product as well as the main temperatures to which they correspond. In our final spectrum charts, not all of the

15 emission lines are used. First, there are two pairs of emission lines corresponding to the same temperature. One pair is Fe xvi 33.54 nm and Fe xvi 36.08 nm, and the other is Fe x 17.72 nm and Mg ix 36.81 nm. For the latter pair, we exclude the line Mg ix 36.81 nm, as most emission lines are from iron ions. For the former, we use the CHIANTI atomic database (version 6.0.1, Dere et al. 1997, 2009) to determine which one is better for our purpose. Based on the CHIANTI database, we may estimate the temperature responses of bound-bound emission lines. The main procedure for CHIANTI is “CH_SYNTHETIC.PRO” in the solar software (SSW, <http://www.lmsal.com/solarsoft/>). For different features on the Sun, the results from CHIANTI are slightly different. Here, we set the electron number density to be

10^{11} cm^{-3} (Milligan et al. 2012b), and assume the abundance for the solar corona and the region for active regions, where the most flares originate. The left and middle panels of Figure 1 show the temperature response curves of the wavelength ranges from 33.47 to 33.61 nm and from 36.02 to 36.20 nm, where the two lines Fe XVI 33.54 nm and Fe XVI 36.08 nm located. It is obvious within the wavelength range of 33.47–33.61 nm that the emission from Fe XVI 33.54 nm is highly pronounced, whereas within the wavelength range of 36.02–36.20 nm, the main ion is Mn XV. Thus, the line Fe XVI 36.08 nm is excluded in constructing our spectrum charts.

Second, we further remove the emission lines significantly blended with multiple ions. As an example, the right panel of Figure 1 shows the temperature response curve for the emission within the range of 17.63–17.83 nm. Although Fe X 17.72 nm makes the main contribution within the wavelength range, its contribution is less than 48% of the total emission, and the emission from Ni XV 17.67 nm, which corresponds to the log temperature of 6.40, is also very strong. Here we consider an

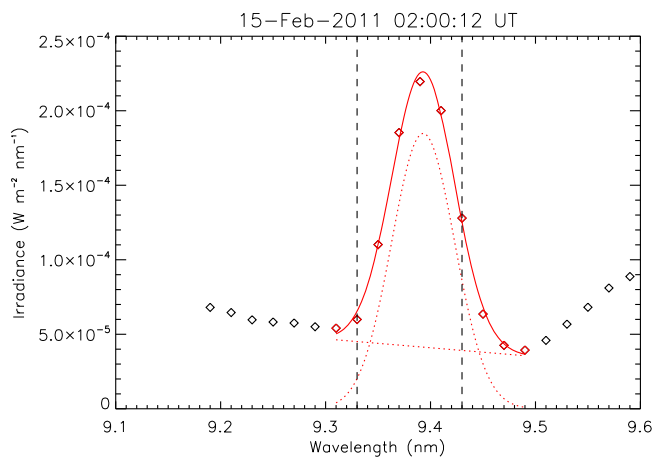


Figure 3. Example showing the EVS line profile around 9.39 nm. The two vertical dashed lines indicate the wavelength range of the line of Fe XVIII 9.39 nm used in the EVL data. The diamonds in red are used in our fitting procedure. The solid curve is the fitting results, which consist of a Gaussian component and a linear component denoted by the dotted lines.

emission line being significantly blended when the contribution of the desired ion is less than 55% of the total emission within the wavelength range. Under this criterion, we remove emission line Nos. 6, 7, 10, 14, and 15 (refer to Table 1), i.e., Fe XIV 21.13 nm, Fe XIII 20.20 nm, Fe X 17.72 nm, He II 25.63 nm, and He II 30.38 nm, from our TDS charts. An example of the final EVE TDS chart constructed based on MEGS-A data is shown in Figure 2, in which 8 emission lines covering the logarithm of temperature from 5.57 to 6.97 are used (marked by the asterisks in Table 1).

2.2. Data Processing

The procedure for generating the TDS chart consists of the following steps.

1. *Extract emission lines.* All eight emission lines selected for TDS (as shown in Figure 2) can be found in the EVL product. In that product, however, the background continuum is not deducted. Thus, we re-extract the lines from the EVS product. At any given time, the spectra data provide the irradiance as a function of wavelength. We use the information provided in the EVL data to secure the wavelength range of each emission line of interest in the EVS data, and then use a linear combination of a Gaussian and a linear function to fit the line profile. To avoid any possible contamination from neighboring lines, only the data points from the nearest local minimum on the left-hand side of the line peak to the nearest local minimum on the right-hand side of the peak are selected for the fitting. Figure 3 shows an example. We treat the linear component of the fitting as the background continuum at this particular time for the line of interest, and subtract it from the total irradiance within the wavelength range of interest. This procedure is applied for all of the selected emission lines at all times. The resultant data are then used for the next step for TDS construction.

2. *Smooth data.* The noise, regardless of instrument noise or small irradiance variations from the full-Sun measurements, of the EVE level 2 data is significant at the cadence of 10 s. Thus, the second step is to reduce the noise by smoothing data. To evaluate the level of noise, we calculate the variance of the data

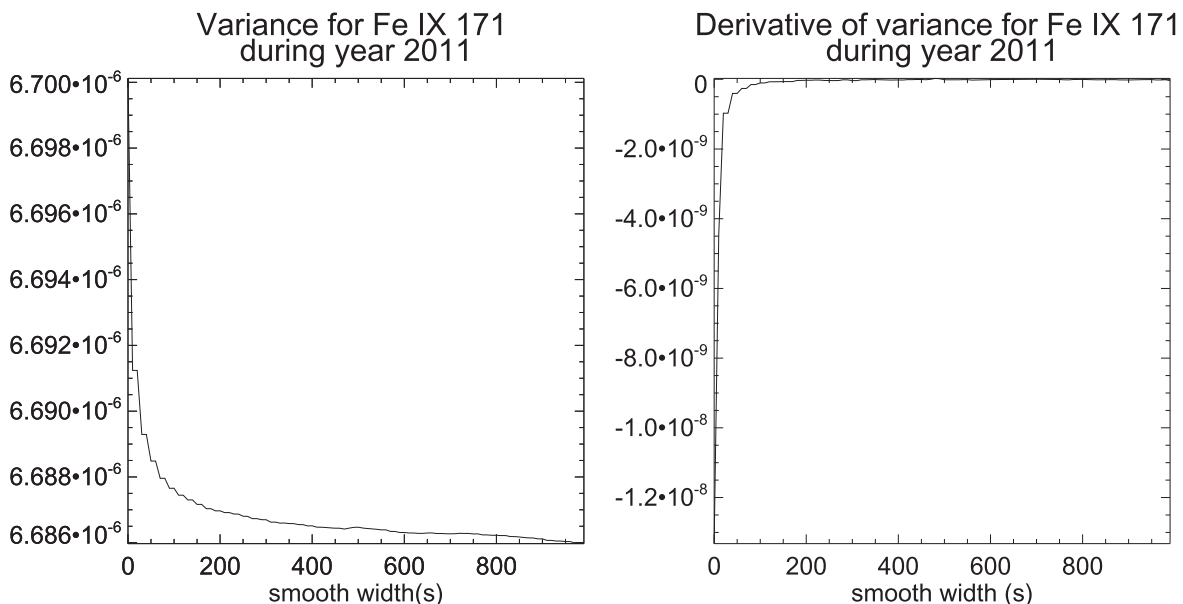


Figure 4. Dependence of the variance (left panel) of Fe IX 17.1 nm emission intensity during the year 2011 and its derivative (right panel) on the smooth width.

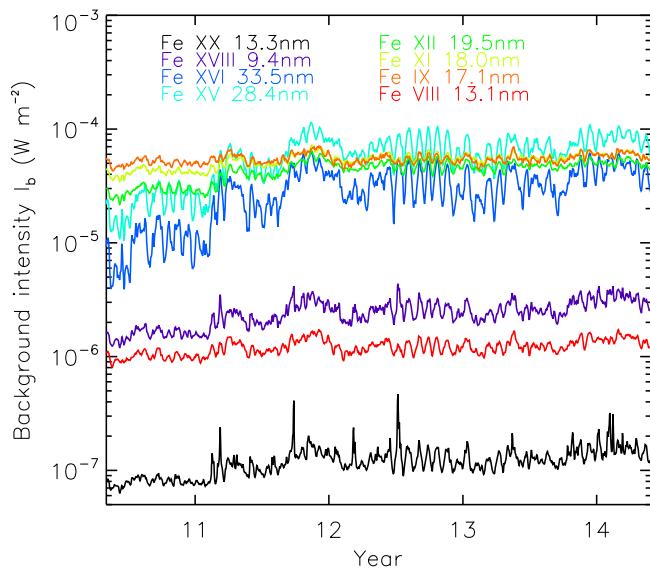


Figure 5. Background emission intensity of the eight selected emission lines.

in the year 2011. Figure 4, for example, shows the variance of the emissions of Fe IX 17.11 nm as well as the derivative of the variance. From the plots, we can see that the variance drops dramatically as the smooth width increases from 10 to 120 s, and then the drop slows down. Thus, we choose a two-minute window to smooth the data. The smoothed data is labeled as $I(t, \lambda)$, in which t is the time with a cadence of 10 s, and λ is the wavelength of one of the eight selected emission lines. It should be noted that although the smoothed data still has a cadence of 10 s, some features on a timescale shorter than two minutes may have been wiped away.

3. *Quantify solar background.* What we care about is the variability of the emission intensity during solar activities, e.g., solar flares. To isolate the solar flare variability from the rest of the solar variations (e.g., solar cycle, solar rotation, active region evolution, etc.), we estimate the background emission and subtract it from the smoothed data. For a solar eruption, the timescale is on the order of hours, so for any given time the background emission of an emission line of interest is set to be the median value of the intensity of this line for the past 48 hr.

Table 2
Four Flares of Interest^a

No.	GOES SXR					EVE TDS				Ref.
	Date	Begin UT	Peak UT	Dur. Min.	Class	Begin UT	Peak UT	LP UT	Dur. Min.	
C1	2011 Sep 08	15:32	15:46	20	M6.7	15:32	15:48	No	~40	...
C2	2010 Nov 05	12:43	13:29	83	M1.0	13:15	13:32	16:42	>300	W11, C12, L15
E1	2011 Mar 08	03:37	03:58	48	M1.5	13:40	14:17	No	~100	Z12, R13
E2	2010 Oct 16	19:07	19:12	5	M3.0	19:09	19:13	20:26	>110	W11, L13, R13

Note.

^a The first column indicates whether the flare was confined or eruptive. The next five columns list the flare parameters based on GOES SXR reports, and the next four columns are based on EVE TDS charts. In columns 5 and 10, “Dur.” means duration in units of minutes. In column 9, “LP,” lists the peak time of the late phase, if any. The last column lists the references in which the flares were investigated. W11 refers to Woods et al. (2011), C12 to Chamberlin et al. (2012), Z12 to Zhang et al. (2012), L13 to Liu et al. (2013), R13 to Ryan et al. (2013), and L15 to Liu et al. (2015).

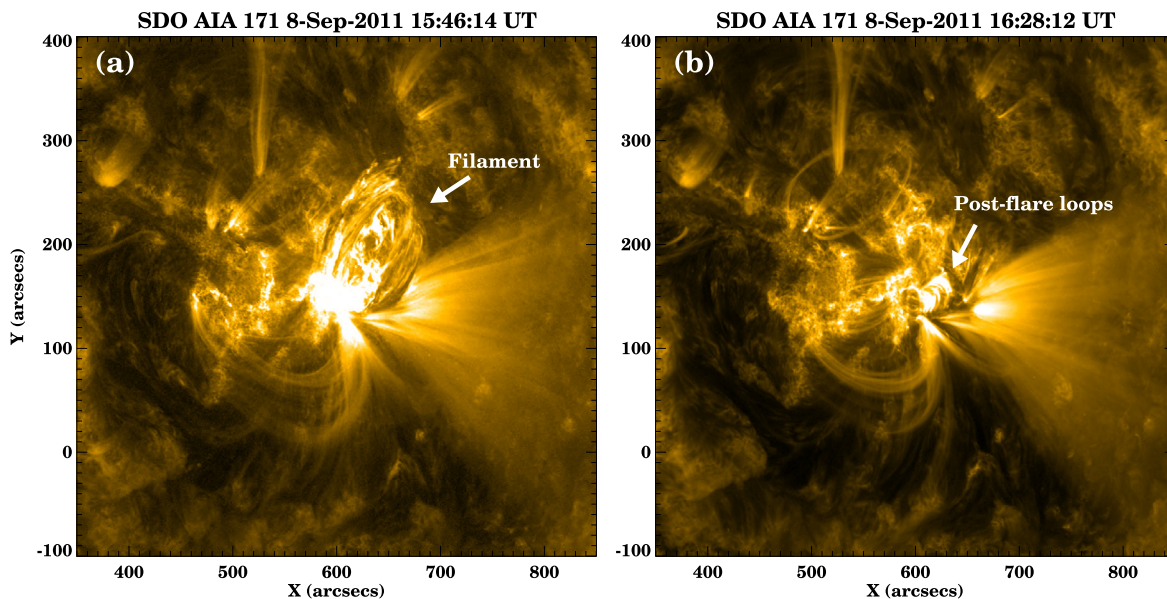


Figure 6. SDO/AIA 171 images of the 2011 September 8 flare (Case C1) at and after the peak time.

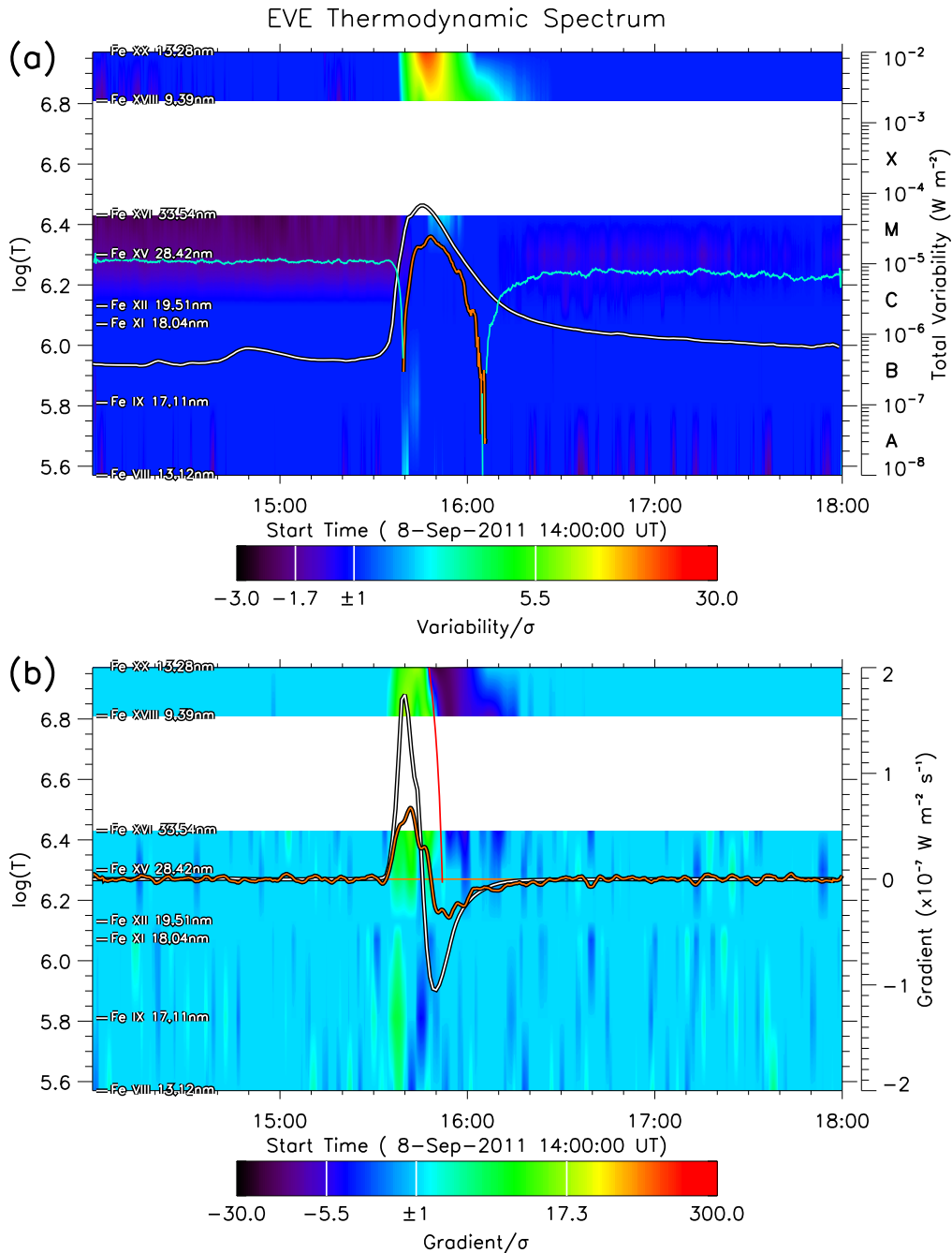


Figure 7. EVE TDS charts for case C1, the 2011 September 8 flare. All the symbols have the same meanings as those in Figure 2 except the red line in panel (b), which is given by fitting the linear cooling. The cyan curve of the total variability in panel (a) indicates a dimming, i.e., the variability is less than zero.

Thus, the background is also a function of time and wavelength, $I_b(t, \lambda)$. Figure 5 displays the intensities of the background emission for reference. Obviously, this method of background emission calculation could be operated automatically and is very useful for statistical studies. However, the obtained background emissions may sometimes be contaminated by preceding flares, particularly when there are many flares within the 48 hr prior to the event of interest.

4. *Calculate variability and the deviation.* The variability is defined as $I_v(t, \lambda) = I - I_b$. It gives the intensity of an activity with the background emission subtracted. The value of the variability could be positive, I_{v+} , or negative, I_{v-} . It is found during the same event that the variability of different emission

lines is quite different, which means that the sensitivities of the emission lines to solar activities are different. To measure the sensitivities of the emission lines and make a uniform standard crossing various events, we calculate the deviations of the positive and negative variabilities away from zero, respectively, by using the entire data from 2011, i.e., $\sigma_{I\pm}(\lambda) = \sqrt{\frac{1}{N-1} \sum_t I_{v\pm}^2(t, \lambda)}$, in which N is the number of data points in the time sequence. The values of $\sigma_{I\pm}$ have been listed in Table 1, from which we can find that the lines Fe xv 28.42 nm and Fe xvi 33.54 nm are the most sensitive to solar activities among the eight emission lines, and line Fe viii 13.12 nm is the least sensitive.

By normalizing the variability, $I_{v\pm}$, by the deviation, $\sigma_{I\pm}$, different emission lines can be compared. We plot the

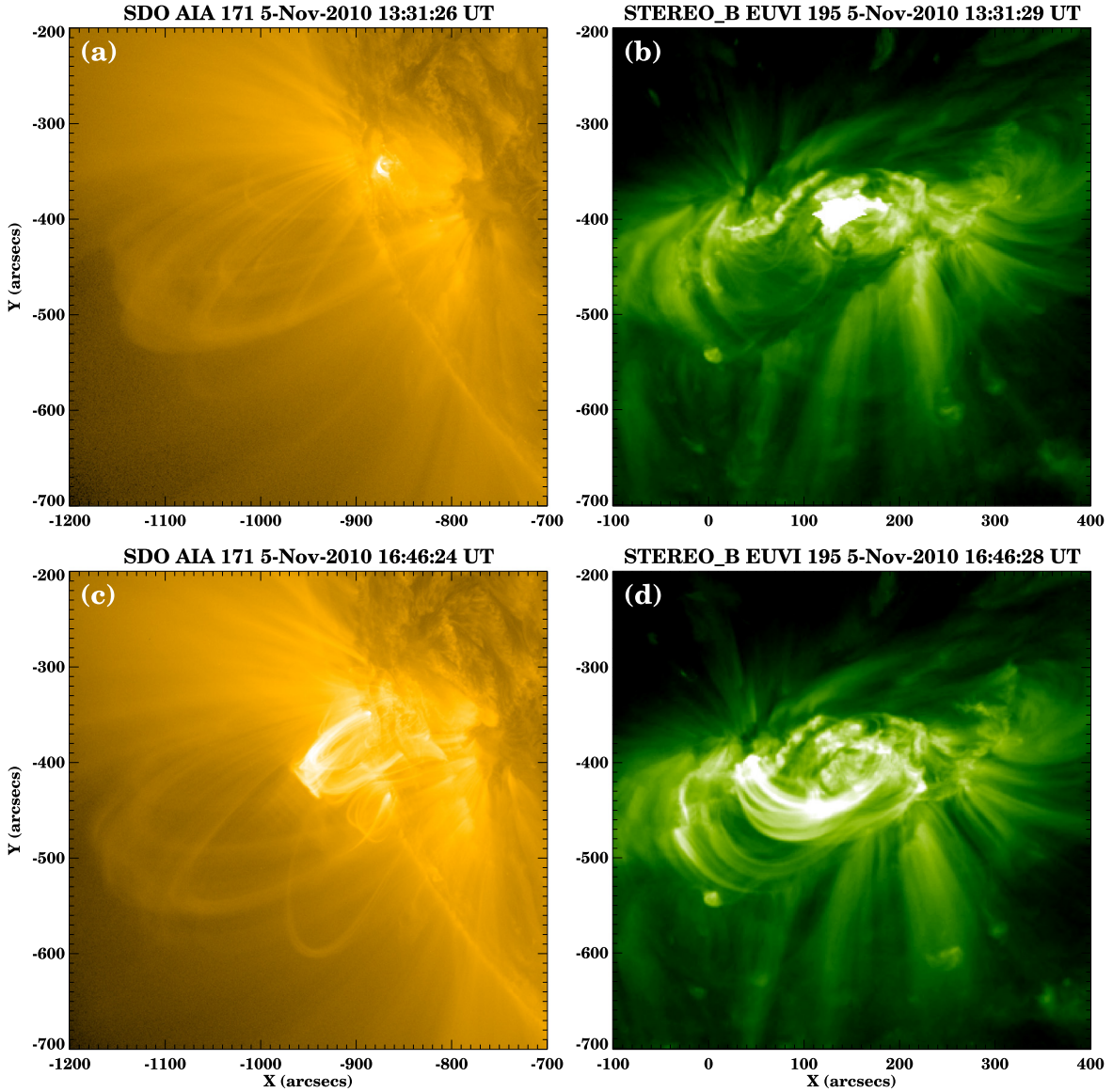


Figure 8. Upper panels show the side and top views of the 2010 November 5 flare near the peak time of the main phase from the *SDO/AIA* 171 (left panel) and *STEREO-B/EUVI* 195 (right panel). The lower panels are snapshots near the peak time of the late phase.

normalized variability in the time-temperature plane to generate the TDS chart, as shown in the upper panel of Figure 2. The small gaps between the selected lines (or temperatures), except for the large one between $\log(T)$ of 6.81 and 6.43, are simply filled by applying linear interpolation. The total variability, $\sum_{\lambda} I_v(t, \lambda)$, is superimposed on the chart as the orange line. (Note that due to the logarithmic scale, for the negative total variability, a cyan line is used.) For comparison, the *GOES* SXR flux from the wavelength band of 1–8 Å is superimposed as the white line.

A similar procedure is used to generate the spectrum chart of the gradient of the line intensity. Based on the two-minute smoothed data, we derive the gradient, $G_{\pm}(t, \lambda) = \frac{dI(t, \lambda)}{dt}$, by linearly fitting the intensity, $I(t, \lambda)$, within a time window of five minutes. Then we calculate the deviations of the gradients away from zero by using the entire data from 2011, i.e., $\sigma_{G_{\pm}}(\lambda) = \sqrt{\frac{1}{N-1} \sum_t G_{\pm}^2(t, \lambda)}$, and plot the chart in the

logarithm of $\frac{G_{\pm}}{\sigma_{G_{\pm}}}$, as shown in the lower panel of Figure 2. The gradient of the total variability is indicated by the orange line, and the gradient of the *GOES* SXR flux by the white line.

An online website has been established to exhibit the TDS charts (<http://space.ustc.edu.cn/dreams/shm/tds>). From the TDS charts, we can learn the start and end times of the enhanced/reduced emissions, the temperatures at which the emissions enhance/reduce, the drift rate of the temperature, the rising and declining rates of the enhancement/reduction, etc. Particularly the relative variability, i.e., the radiative output with the background deducted, of EUV emission provides us information to reveal the plasma thermodynamics in the middle to high corona, and may also be useful in studying changes in the Earth's atmosphere as well as its associated physics mechanisms, which is partially driven by, e.g., solar flares (e.g., Sutton et al. 2006; Pawlowski & Ridley 2008; Qian et al. 2010).

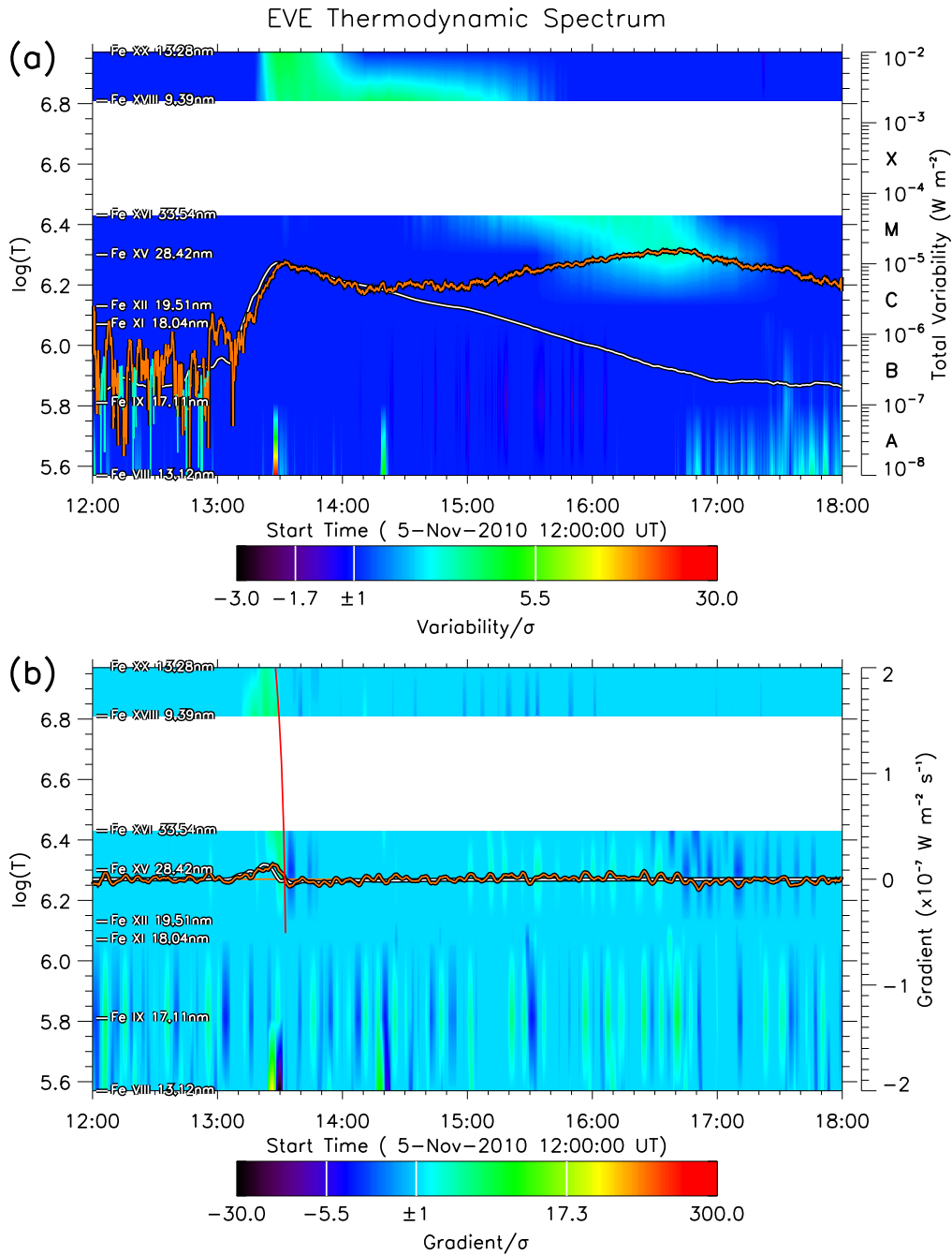


Figure 9. EVE TDS charts for case C2, the 2010 November 5 flare.

3. FOUR DIFFERENT TYPES OF FLARES

Traditionally, flares are classified as confined and eruptive flares. The former is not associated with a coronal mass ejection (CME) and the latter is. Recently, *SDO* observations reveal that flares may not only have one main phase of emission, but also experience a late phase, i.e., there is a second peak of the flare emission (Woods et al. 2011). Combining the two different features, we may classify the flares as confined/eruptive flares with/without a late phase. In the following sections, we will present four M-class flares in these four different types. The four flares with the exception of the first one have all been studied previously, as listed in Table 2. By investigating these flares, we justify our method and also show the flare signatures in the TDS charts.

3.1. A Confined Flare on 2011 September 8

Based on the *GOES* SXR flux, the 2011 September 8 flare is an M6.7 X-ray flare, starting at 15:32 UT and peaking at 15:46 UT, and the entire duration of the flare is 20 minutes. Figures 6(a) and (b) show the *SDO/AIA* 171 images at and after the peak of the flare. It occurred in a compact region in the western hemisphere. An active region filament rose during the flare but did not erupt out, and post-flare loops were clear. There was no dimming in the EUV images and no CME observed by *SOHO/LASCO* (Brueckner et al. 1995), suggesting a confined flare.

In the EVE TDS chart, there were clear enhancements during the flaring period, as shown in Figures 7(a) and (b). During the same period, there was no other flare on the visible solar disk,

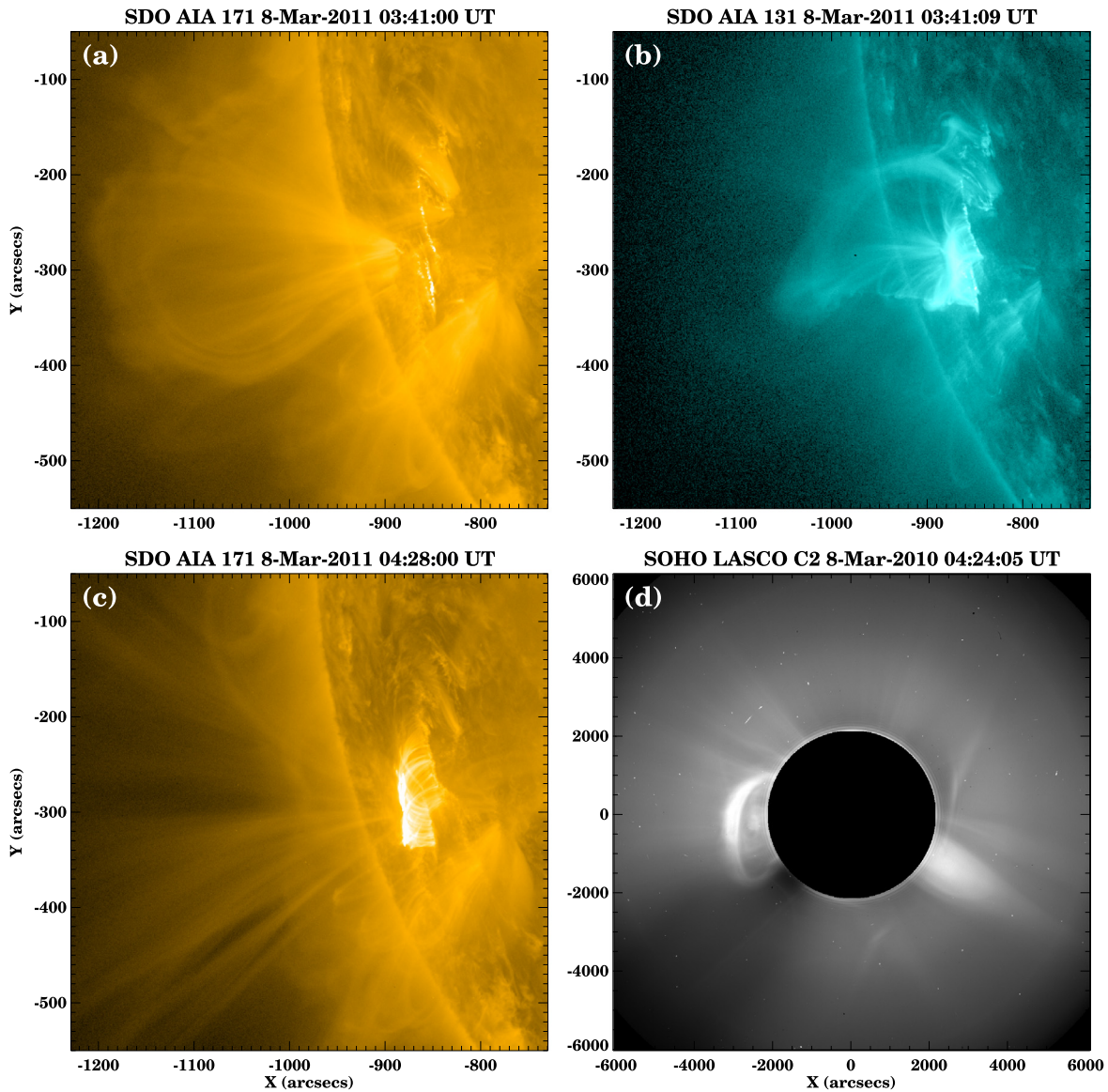


Figure 10. Upper panels show the arcades viewed in *SDO/AIA* 171 (left panel) and the flux rope underneath viewed in *SDO/AIA* 131 (the right panel) during the rising phase of the 2011 March 8 flare. Panel (c) shows the post-flare loops after the peak time. Panel (d) displays the associated CME observed by *SOHO/LASCO* C2.

and therefore the features displayed in the spectrum chart reflect the thermal processes of the flare. First, the flare heated the coronal lines simultaneously, and the emission enhancements of the lines at high temperatures were more significant than those at low temperatures. The start time is defined by the significant deviation from zero of the orange curve in the gradient chart (Figure 7(b)), which is around 15:32 UT, the same as reported for *GOES* SXR. The peak time is about 15:48 UT, two minutes later than that of *GOES* SXR (reading from the curves in Figure 7(a)), reflecting the timescale of the cooling process of extremely hot X-ray emission plasma to less hot EUV plasma. For a *GOES* X-ray flare, the end time is traditionally defined as when the current SXR flux returns to half of the peak flux.⁶ Here we define the end time of a flare as the time when the gradient indicated by the orange curve in Figure 7(b) returns to zero. Due to the different definitions, our

estimated duration of the flare, which is about 40 minutes, is much longer than that from the *GOES* report.

Second, the cooling process of the heated thermal plasmas at high temperatures are notable in both the variability and gradient charts. In particular, the cooling is clearly revealed by the drift of the interface between the positive and negative gradients, as shown in the gradient chart (Figure 7(b)). The drift rate characterizes the overall cooling rate of the flare plasma that is a combined effort of radiative cooling and conductive cooling. By using the linear function, i.e., $T = T_0 + c_r t$, to fit the interface, we can estimate that the linear cooling rate, c_r , is about $-0.03 \pm 0.01 \text{ MK s}^{-1}$ for the heated plasma. When fitting, we set the uncertainty in temperature to be ± 0.15 in $\log(T)$, which is approximately the FWHM of the main peak of the temperature response curve for all of the selected emission lines. The red curve in Figure 7(b) shows the fitting result. It should be noted that the estimated cooling rate is a lower limit because most flares continuously release magnetic energy and

⁶ Refer to <http://www.ngdc.noaa.gov/stp/solar/solarflares.html>.

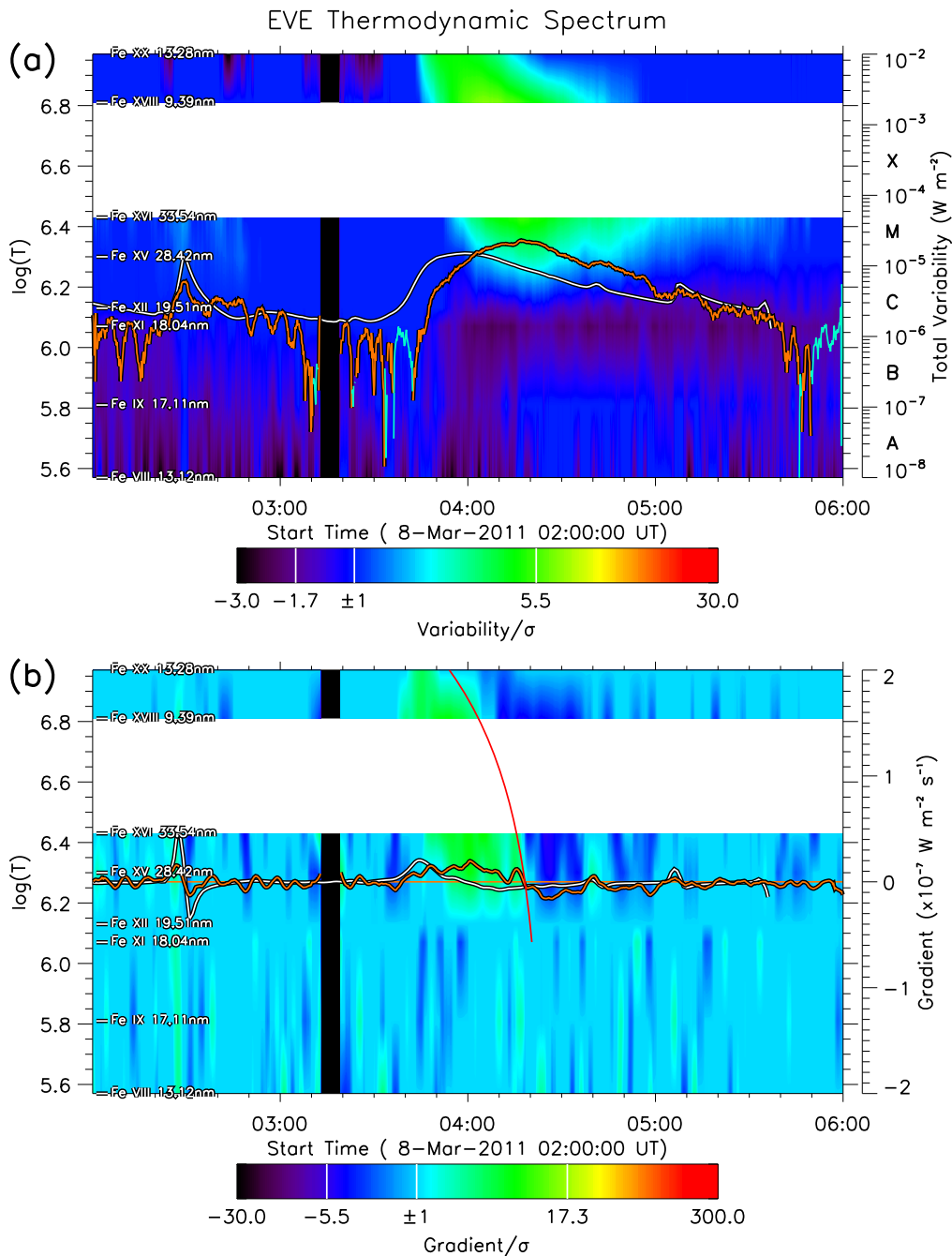


Figure 11. EVE TDS charts for case E1, the 2011 March 8 flare.

heat the plasmas throughout the entire phase (e.g., Jiang et al. 2006; Warren 2006; Ryan et al. 2013).

There was no late phase associated with this flare. Besides, one may notice that the variability chart shows a significant dimming, i.e., the decrease of the emissions, before the flare (the dark region near $\log(T)$ of 6.2–6.4 in Figure 7(b)). It is not caused by any solar activity, but is the consequence of a bright active region on the west limb rotating off from the visible solar disk.

3.2. A Confined Flare with a Late Phase on 2010 November 5

This flare was studied by Woods et al. (2011), Chamberlin et al. (2012), and Liu et al. (2015). It started at 12:43 UT,

peaked at 13:29 UT, and lasted 83 minutes according to the *GOES* report. The flare has a much longer decay phase than the previous flare. Its main phase occurred in a compact region (Figures 8(a) and (b)), but the late phase was due to the brightening of the neighboring loops in a larger region (Figures 8(b) and (c)). Although the flare is as intense as M1.0 and is long lasting, no CME was associated.

The main and late phases of the flare are clearly shown by the total variability in Figure 9(a). The peak of the late phase is higher than that of the main phase, suggesting that additional magnetic and/or kinetic energies were converted into thermal energy during the late phase, which was even larger than that during the main phase. However, the *GOES* SXR did not show any signature of the late phase, further implying that the energy

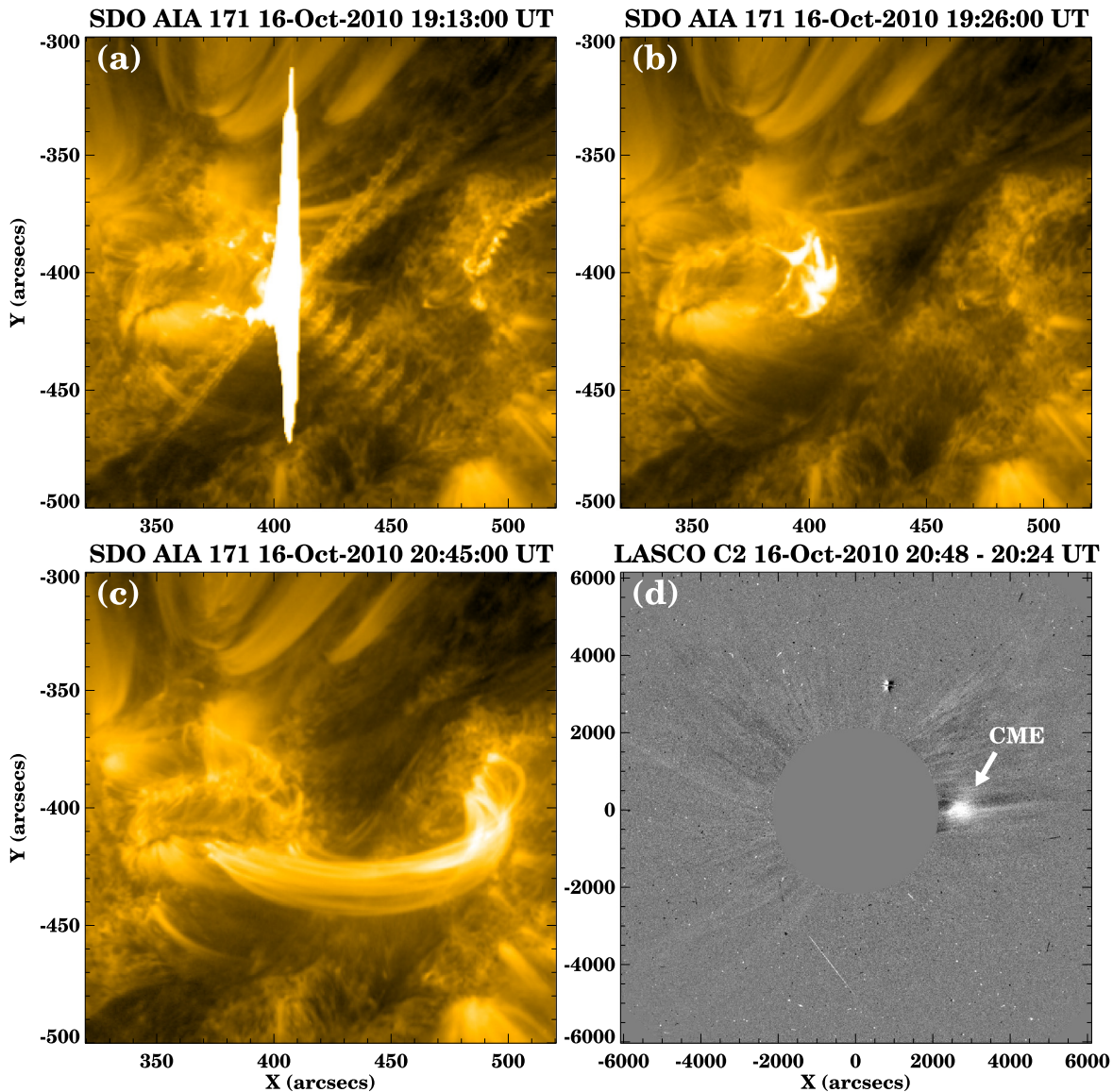


Figure 12. Panels (a)–(c) show the peak time, decline phase, and late phase of the 2010 October 16 flare viewed by *SDO/AIA* 171. Panel (d) displays the associated weak CME observed by *SOHO/LASCO* C2.

conversion during the late phase was probably via a much gentler way than that during the main phase.

Based on the spectrum charts, the flare began at about 13:15 UT and ended after 18:30 UT (exceeding the time range of the charts), and the first and second peaks occurred around 13:32 and 16:42 UT, respectively. Compared with the *GOES* SXR, the peak time of the main phase is about three minutes late, which is similar to the previous case, and the duration of the flare in EUV passbands is much longer than that in SXR. Such a long-duration confined flare is contrary to the traditional picture that long-duration flares tend to be eruptive (e.g., Harrison 1995; Yashiro et al. 2006), implying a strong constraint above the flare region (e.g., Wang & Zhang 2007; Liu 2008). Another case could be found in the paper by Liu et al. (2014), who reported a long-duration confined X-class flare.

At the beginning of the flare, the plasma was mainly heated at a high temperature above 6.3 MK, and then the enhancement apparently drifted down to around 2.0 MK when the second peak occurred. Since the enhanced emissions in the main and

late phases came from the different regions, as indicated in Figures 8(a) and (b), the drift feature in Figure 9(a) cannot be interpreted as a coherent cooling process. Actually, it is a combination of a cooling process during the main phase and an additional heating and cooling process during the late phase. The cooling signature during the main phase could be clearly recognized in the gradient chart (as indicated by the red linear fitting line in Figure 9(b)), from which the linear cooling rate is estimated as about -0.03 ± 0.01 MK s^{-1} .

3.3. An Eruptive Flare on 2011 March 8

The flare, which started at 03:37 UT and peaked at 03:58 UT on 2011 March 8, was associated with the eruption of a flux rope (Zhang et al. 2012). The flux rope and the overlying arcades can be seen in the AIA 131 (Figure 10(b)) and AIA 171 (Figure 10(a)) images, respectively. The flux rope developed into a CME that was recorded by the *SOHO/LASCO* C2 camera as shown in Figure 10(d). The post-flare loops are clearly visible after the flux rope erupted (Figure 10(c)).

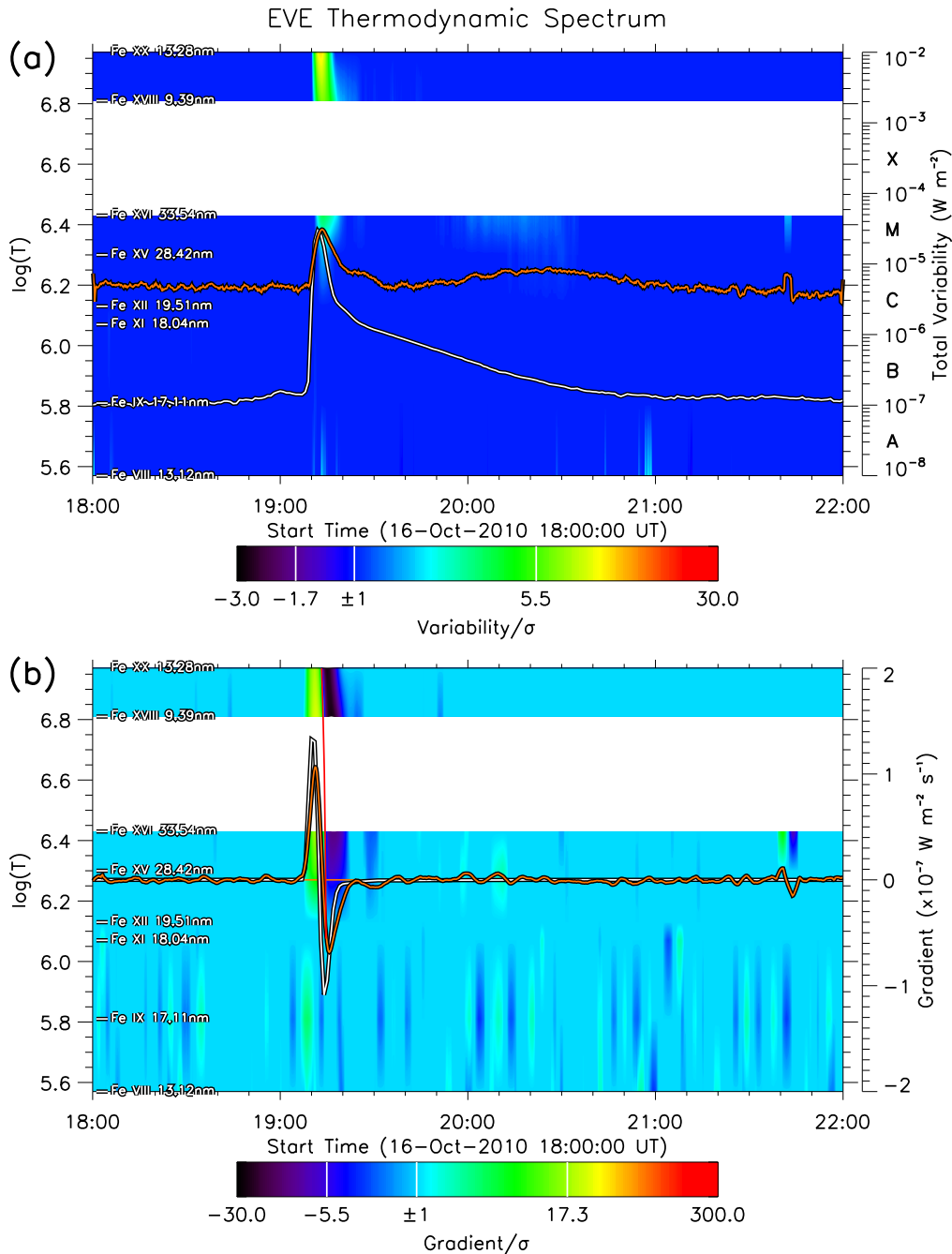


Figure 13. EVE TDS charts for case E2, the 2010 October 16 flare.

Based on the *GOES* SXR, it is an M1.5 flare and the duration is about 48 minutes. On the other hand, as we can see in Figure 11(a), the entire profile of the variability curve of the flare lags about 10–30 minutes behind the SXR curve. The flare began at about 03:40 UT, peaked at 04:17 UT, and ended after 05:20 UT in the EUV passbands. The EUV peak is about 19 minutes later than the SXR peak. The delay is much longer than those in the other cases, but is consistent with the slow cooling rate of the heated plasma during the flare, as will be seen below. Besides, under our definition, the duration of the flare is more than 100 minutes in the EUV, suggesting a long-duration flare.

In contrast to the previous cases, the enhancement of the EUV emission appeared earlier at the higher temperature, and a clear drift of the enhancement, which forms a flag shape, could be found in Figure 11(a). There was no significant enhancement

at low temperatures. By using the gradient chart (Figure 11(b)), we find that the linear cooling rate of the heated plasma is about $-0.005 \pm 0.002 \text{ MK s}^{-1}$, about one order lower than the two previous cases.

Besides, the variability chart (Figure 10(a)) suggests that there are significant dimmings before and during the flare below the temperature of $\log(T) < 6.2$. These dimmings are all probably due to the depletion of the coronal density caused by eruptions. The dimming before the flare is associated with an M3.7 flare peaking at 20:01 UT on the previous day.

3.4. An Eruptive Flare with a Late Phase on 2010 October 16

This is an impulsive M3.0 flare based on the report of *GOES* SXR. It started at 19:07 UT and peaked at 19:12 UT

Table 3
X-ray Flares Equal to or Greater than M5.0 from 2010 May to 2014 May^a

No.	Date		SXR		TDS		Peak delay (minute)	Type	No.	Date	SXR		TDS		Peak delay (minute)	Type	
	Time (UT)	Class	Time (UT)	Class	Time (UT)	Class					Time (UT)	Class	Time (UT)	Class			Time (UT)
1	2010 Nov 06	15:36	M5.4	M4.1	15:41	M4.1	-0.036	4.8	II	38	2012 Oct 20	18:14	M9.1	M3.7	-0.062	2.2	II
2	2011 Feb 13	17:38	M6.6	M4.3	17:41	M4.3	-0.041	2.9	II	39	2012 Oct 22	18:51	M5.1	M1.8	-0.027	2.0	II
3	2011 Feb 15	01:56	X2.3	M9.0	01:58	M9.0	-0.032	2.2	...	40	2012 Oct 23	03:17	X1.7	M3.8	-0.087	2.0	II
4	2011 Feb 18	10:11	M6.6	M3.5	10:13	M3.5	-0.080	1.7	II	41	2012 Nov 13	02:04	M6.1	M3.6	-0.069	1.8	...
5	2011 Mar 08	10:44	M5.4	M1.7	10:47	M1.7	-0.047	3.1	...	42	2013 Apr 11	07:16	M6.5	M5.8	-0.007	8.8	I
6	2011 Mar 09	23:23	X1.6	M8.0	23:27	M8.0	-0.024	3.6	I	43	2013 May 03	17:32	M5.7	M3.9	-0.052	1.4	...
7	2011 Jul 30	02:09	M9.3	M6.2	02:10	M6.2	-0.101	1.4	...	44	2013 May 13	02:16	X1.7	M5.8	-0.016	3.6	II
8	2011 Aug 03	13:47	M6.1	M5.0	13:49	M5.0	-0.018	1.8	I	45	2013 May 13	16:05	X2.9	M6.5	...	1.6	II
9	2011 Aug 04	03:57	M9.3	M7.4	04:00	M7.4	-0.030	3.4	I	46	2013 May 14	01:11	X3.2	X1.1	-0.056	2.2	II
10	2011 Aug 09	08:05	X7.0	X1.9	08:06	X1.9	-0.066	1.4	II	47	2013 May 15	01:48	X1.3	M7.1	-0.024	5.4	...
11	2011 Sep 06	01:50	M5.4	M2.8	01:51	M2.8	...	1.1	II	48	2013 May 22	13:32	M5.0	M5.1	-0.006	15.9	I
12	2011 Sep 06	22:20	X2.1	M9.6	22:22	M9.6	-0.069	1.9	...	49	2013 Jun 07	22:49	M6.0	M3.0	...	0.5	II
13	2011 Sep 07	22:38	X1.8	M8.0	22:41	M8.0	-0.066	3.1	II	50	2013 Oct 24	00:30	M9.4	M7.3	-0.024	4.6	I
14	2011 Sep 08	15:46	M6.7	M2.4	15:48	M2.4	-0.017	2.2	...	51	2013 Oct 25	08:01	X1.7	M4.5	-0.049	2.9	II
15	2011 Sep 22	11:00	X1.5	M5.2	11:05	M5.2	...	5.1	I	52	2013 Oct 25	15:03	X2.1	M5.9	-0.019	0.6	II
16	2011 Sep 24	09:40	X1.9	M5.5	09:44	M5.5	-0.040	4.0	II	53	2013 Oct 28	02:03	X1.0	M4.4	...	2.8	I
17	2011 Sep 24	13:17	M7.1	M5.4	13:37	M5.4	-0.006	19.8	I	54	2013 Oct 28	04:41	M5.1	M1.6	-0.030	2.1	...
18	2011 Sep 24	20:36	M5.8	M2.6	20:38	M2.6	-0.116	2.0	...	55	2013 Oct 29	21:54	X2.3	M4.3	-0.036	1.6	I
19	2011 Sep 25	04:50	M7.5	M5.2	04:54	M5.2	-0.016	4.5	...	56	2013 Nov 01	19:53	M6.3	M4.3	-0.046	2.5	II
20	2011 Nov 03	20:27	X2.0	M7.0	20:29	M7.0	...	2.3	...	57	2013 Nov 03	05:22	M5.0	M3.2	-0.107	1.8	II
21	2012 Jan 23	03:59	M8.8	M8.1	04:12	M8.1	-0.011	12.9	I	58	2013 Nov 05	22:12	X3.4	M7.7	-0.059	2.1	II
22	2012 Jan 27	18:36	X1.8	X1.1	18:48	X1.1	-0.013	12.4	I	59	2013 Nov 08	04:26	X1.1	M4.9	-0.072	1.3	II
23	2012 Mar 05	04:05	X1.1	M6.8	04:16	M6.8	...	10.5	I	60	2013 Nov 10	05:14	X1.1	M6.4	-0.037	1.0	I
24	2012 Mar 07	00:24	X5.4	X1.6	00:27	X1.6	...	3.1	I	61	2013 Nov 19	10:26	X1.0	M2.9	-0.044	4.0	II
25	2012 Mar 09	03:53	M6.4	M6.1	04:01	M6.1	-0.014	7.9	...	62	2013 Dec 31	21:58	M6.5	M4.7	...	2.2	...
26	2012 Mar 10	17:44	M8.5	M5.3	17:53	M5.3	...	9.1	I	63	2014 Jan 01	18:52	M9.9	M6.9	-0.050	2.5	...
27	2012 May 10	04:18	M5.8	M3.0	04:19	M3.0	-0.117	0.9	II	64	2014 Jan 07	10:13	M7.2	M3.5	-0.064	2.9	...
28	2012 May 17	01:47	M5.1	M4.2	01:58	M4.2	-0.011	11.4	I	65	2014 Jan 07	18:30	X1.2	X1.1	-0.008	15.6	I
29	2012 Jul 02	10:52	M5.6	M5.2	10:54	M5.2	-0.024	2.2	...	66	2014 Jan 30	16:11	M6.7	M5.3	-0.005	26.5	I
30	2012 Jul 04	09:55	M5.4	M3.5	09:57	M3.5	-0.056	1.9	II	67	2014 Feb 04	04:00	M5.2	M3.1	-0.009	2.7	...
31	2012 Jul 05	11:44	M6.2	M2.5	11:47	M2.5	-0.057	3.1	...	68	2014 Feb 25	00:49	X5.0	X1.2	-0.036	8.6	I
32	2012 Jul 06	23:08	X1.1	M4.7	23:10	M4.7	-0.056	1.7	...	69	2014 Mar 12	22:34	M9.4	M2.0	-0.066	2.0	II
33	2012 Jul 08	16:32	M6.9	M2.9	16:38	M2.9	-0.030	5.6	...	70	2014 Mar 29	17:48	X1.0	M5.4	-0.046	2.6	II
34	2012 Jul 12	16:49	X1.4	M6.9	17:08	M6.9	...	18.8	I	71	2014 Apr 02	14:05	M6.5	M4.3	-0.004	13.3	I
35	2012 Jul 19	05:58	M7.8	M2.0	05:57	M2.0	...	-0.9	I	72	2014 Apr 18	13:03	M7.3	M6.6	-0.012	3.8	I
36	2012 Jul 28	20:56	M6.2	M5.0	20:57	M5.0	-0.010	1.3	...	73	2014 Apr 25	00:27	X1.4	M2.9	-0.014	2.5	II
37	2012 Aug 18	01:02	M5.6	M1.7	01:04	M1.7	-0.043	2.2	II	74	2014 May 08	10:07	M5.3	M2.3	-0.021	4.6	II

Note.

^a In this table, c_r is the linear cooling rate measured from TDS charts through the method introduced in Section 3. For those flares that cannot be simply measured by a linear cooling process, we leave them blank. The column "Peak delay" means the delay time of the EUV peaks with respect to the associated SXR peaks. The column "Type" indicates if the flare shows a clear Type I or II drift in its EVE TDS chart (refer to Section 4.2 for more details).

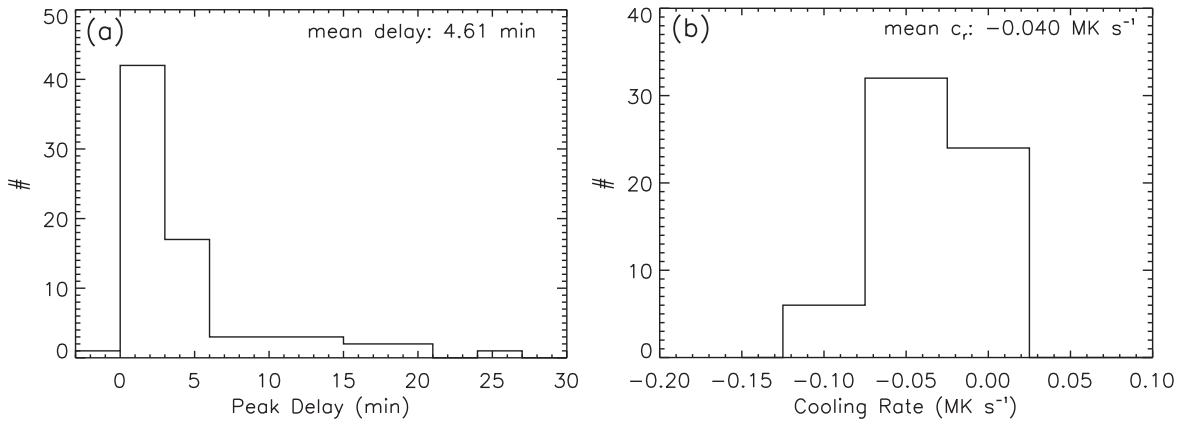


Figure 14. Histograms of the delay times of the EUV peaks with respect to the SXR peaks and the linear cooling rates measured from EVE TDS charts.

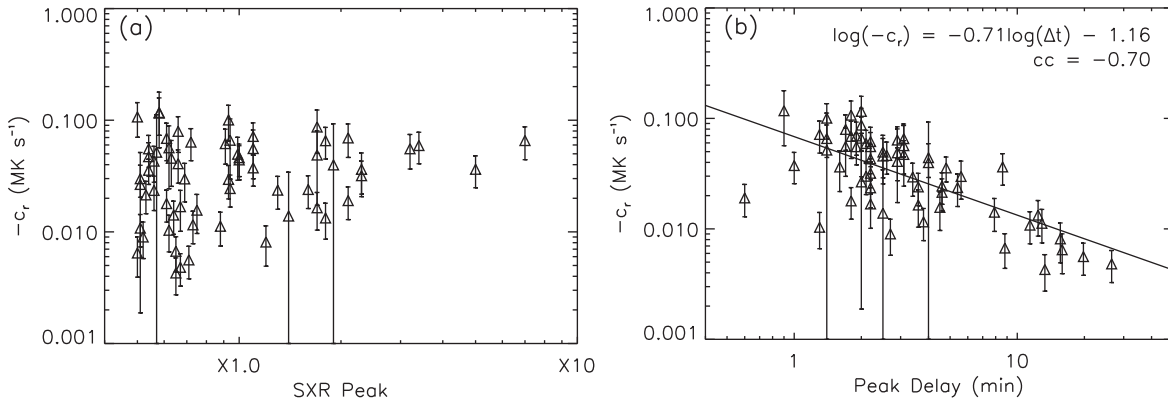


Figure 15. Scatter plots showing (panel (a)) the correlation between the linear cooling rate and the SXR peak intensity and (panel (b)) the correlation between the linear cooling rate and the peak delay time. The solid line in panel (b) is a linear fitting to the logarithm values of the parameters.

(Figure 12(a)). The end time in the *GOES* definition is at the same minute as the peak time, so that the duration of the flare is only five minutes. However, this flare has a late phase, as suggested by Woods et al. (2011) and Liu et al. (2013). The enhancement of the emission during the late phase is attributed to the neighboring loops, as shown in Figure 12(c). This flare was accompanied by a weak CME with post-flare loops clearly visible in the source region (Figures 12(c) and (d)).

The main and late phases of the flare can be clearly seen in Figure 13(a). The main peak occurred at 19:13 UT and the late-phase peak was at 20:26 UT. Compared with the SXR, the main peak in EUV is about one minute late. The start time of the flare in the EUV is about 19:09 UT and the end time is after 21:00 UT, which suggest that the flare actually lasted much longer in the EUV than in the SXR.

From the gradient chart (Figure 13(b)), the drift of the enhancement feature from the high temperature to the low temperature is quite fast. Our fitting suggests that the linear cooling rate is about $-0.10 \pm 0.04 \text{ MK s}^{-1}$. Besides the apparent drift feature in the main phase, we also can find a very faint drift feature from the main phase to the late phase in the variability chart (see Figure 13(a)). As we pointed out before, this drift may not be interpreted merely as a cooling process, but is a manifestation of the additional heating of the plasma in the neighboring loops, as shown in Figure 12(c) (also refer to Liu et al. 2013).

4. STATISTICAL RESULTS ABOUT FLARES EQUAL TO OR GREATER THAN M5.0

4.1. Delay of EUV Peaks and the Cooling Rate

The previous section presented what we can learn from the TDS charts through the investigation of four flares of different types. Here we apply our method to all the flares equal to or greater than M5.0 class. According to *GOES* SXR records, there were about 75 M5.0+ flares during the EVE/MEGS-A's five-year lifetime. All of these flares have EVE observations except one. Table 3 list information about these flares.

The observed linear cooling rate of the heated plasma for the cases in the previous section varies from -0.003 to -0.14 MK s^{-1} . Its value is roughly correlated to the delay of the peaks between the SXR and the EUV emissions. A slower cooling rate tends to have a longer delay time, suggesting a systematic cooling process from tens to a few million Kelvin. However, there were only four data points. To solidify the correlation, we measure the cooling rates of all the M5.0+ flares as well as the delay times of the EUV peaks.

First, it is found that the EUV peak is behind of the SXR peak for all of the flares except one, the 2012 July 19 flare (No. 35 in Table 3), of which the EUV peak is 0.9 minutes ahead of the SXR peak. However, for this event, it does not mean that the EUV emission reaches the peak before the SXR emission, because the time difference is less than one minute, which falls

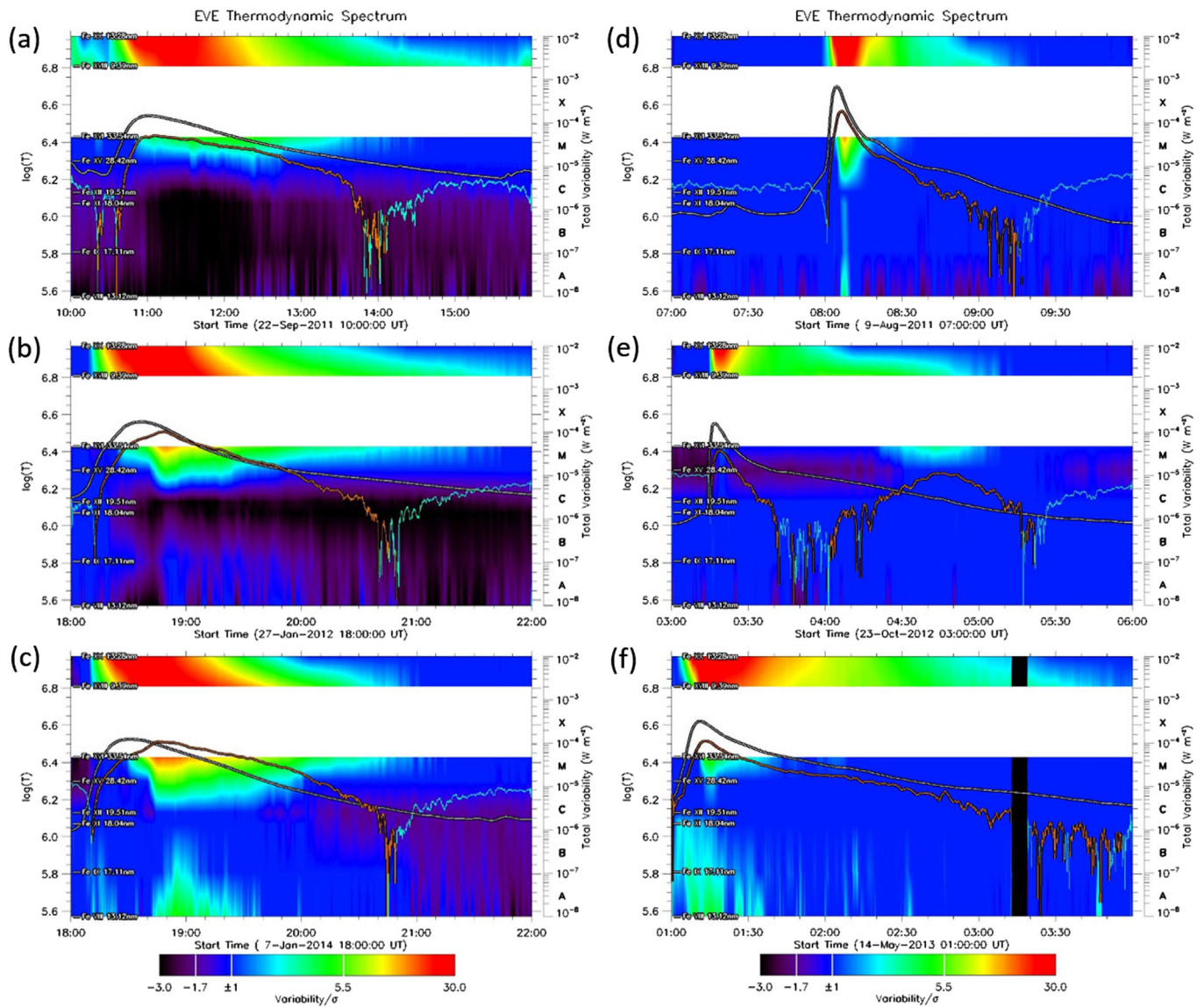


Figure 16. Six example flares showing the Type I drift pattern (left column, panels (a)–(c)) and the Type II drift pattern (right column, panels (d)–(f)).

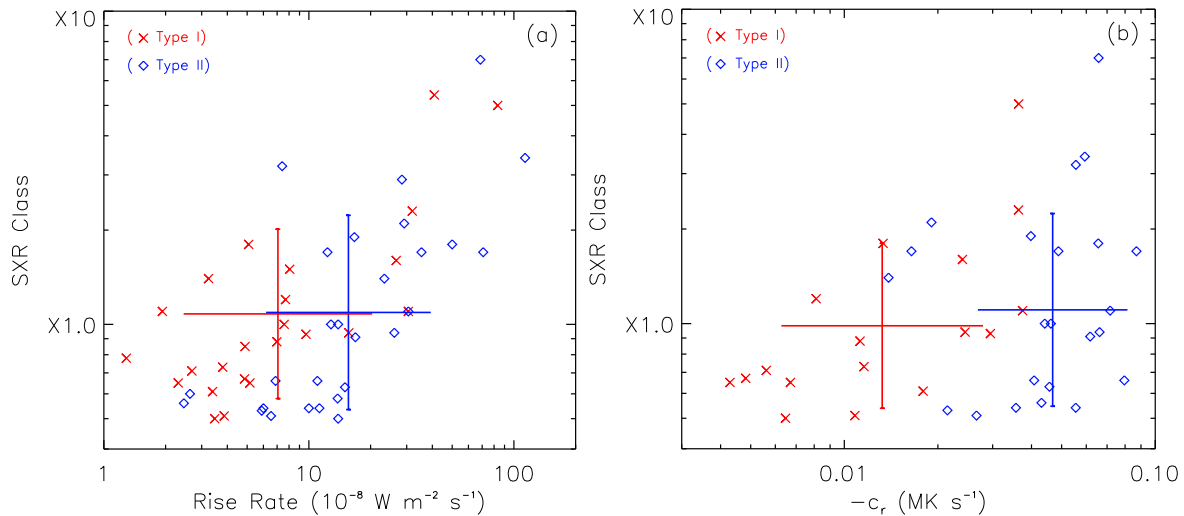


Figure 17. Properties of the flares with different drift patterns (red “x” symbols for Type I and blue diamonds for Type II). Panel (a) shows the scatter plot between the SXR rise rate and its peak intensity, and panel (b) shows the scatter plot between the linear cooling rate and the SXR peak intensity. The crossed vertical and horizontal lines mark the mean values and the error bars for the two sets of data points in the logarithmic scale.

Table 4
Flares with a Clear Late Phase

No.	Date	SXR main phase		TDS main phase		TDS late phase						Eruptive ^a
		Time	Class	Time	Class	Time 1	Peak 1	Time 2	Peak 2	Time 3	Peak 3	
L1	2010 Nov 06	15:36	M5.4	15:41	M4.1	16:38	M2.6	18:09	M2.6	19:28	M2.4	Y
L2	2011 Mar 08	10:44	M5.4	10:47	M1.7	12:16	M1.2	N
L3	2011 Mar 09	23:23	X1.6	23:27	M8.0	00:01	M2.4	N
L4	2011 Sep 07	22:38	X1.8	22:41	M8.0	23:52	C9.3	Y
L5	2011 Sep 24	20:36	M5.8	20:38	M2.6	21:24	M1.8	N
L6	2011 Nov 03	20:27	X2.0	20:29	M7.0	21:02	M3.4	N
L7	2012 Oct 20	18:14	M9.1	18:16	M3.7	19:48	M1.1	21:16	M1.4	Y
L8	2012 Oct 22	18:51	M5.1	18:53	M1.8	19:33	M1.0	20:28	M1.1	N
L9	2012 Oct 23	03:17	X1.7	03:19	M3.8	04:46	M1.2	N
L10	2013 Nov 01	19:53	M6.3	19:55	M4.3	21:51	M1.3	N
L11	2014 Mar 12	22:34	M9.4	22:36	M2.0	00:33	C8.2	N
L12	2014 Apr 25	00:27	X1.4	00:30	M2.9	03:42	C3.4	Y

Note.

^a “Y” means that the flare is associated with a CME, and “N” means there is no CME.

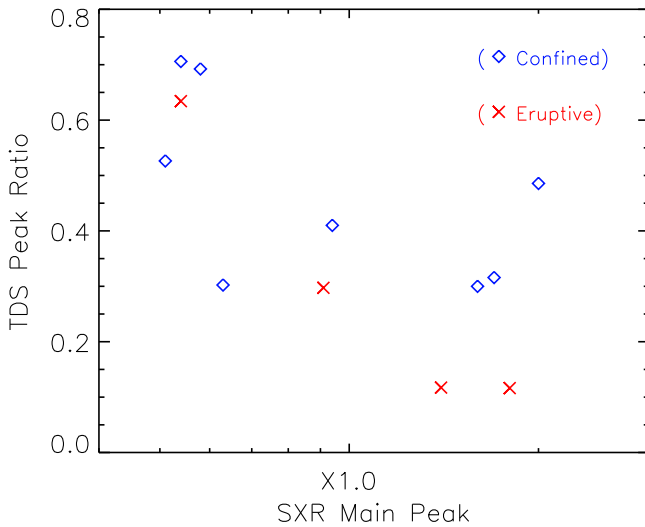


Figure 18. Scatter plot of the 12 late-phase flares. The horizontal axis indicates the flare class defined by the *GOES* SXR, and the vertical axis gives the intensity ratio of the first late-phase peak to the main-phase peak read from the TDS charts. The eruptive flares are marked by red “x” and the confined flares by blue diamonds.

in the uncertainty of the data; our EVE data were smoothed by a two-minute time window and the cadence of the SXR data used here is one minute. The distribution of the delay times in Figure 14(a) shows that the delay for most flares is less than 6 minutes and occasionally longer than 20 minutes, and the mean value of the peak delay is about 5 minutes.

Not all of the flares have a clear cooling process like the events presented in Section 3. Those flares (12 events) present alternate cooling and heating signatures in the TDS charts, so that we do not try to measure their cooling rates. For the rest, the distribution of the cooling rates has been displayed in Figure 14(b). We find that the cooling rate is about -0.04 MK s^{-1} on average, slightly smaller than the mean value of -0.035 MK s^{-1} obtained by Ryan et al. (2013) for M1.0+ flares. This result implies that the stronger flares have a faster cooling process. It can be further confirmed in Figure 15(a), in which the trend of the lower limit of the

cooling rate is clearly shown. In that plot, one can find that the cooling rate of M-class flares could be as slow as -0.004 MK s^{-1} , but that of almost all of the X-class flares are faster than -0.01 MK s^{-1} .

Furthermore, we compare the cooling rates and the delay of the EUV peaks. A strong power-law correlation between them is found, as shown in Figure 15(b). The correlation coefficient is about 0.70. The slower cooling rate does result in a longer delay, confirming the previous speculation that flares experience a coherent cooling process from SXR emission to EUV emission.

4.2. Two Temperature Drift Patterns

By browsing the TDS charts of these M5.0+ flares, we find there are generally two drift patterns. One pattern shows a drift from higher temperature to lower temperature with time between the range of $\log(T)$ of about 6.2 and 7.0, which looks like a quadrilateral. The other pattern shows a somewhat different drift; the strongest emissions look like a triangle. In our sample, 52 flares clearly show such different patterns (as indicated in Table 3). Figure 16 gives three examples for each pattern. For convenience, we call the two patterns Type I and II, respectively. The direct cause of the two types of drift patterns is obvious. For the Type I flares, the enhanced emission from the higher temperature line of Fe xx 13.28 nm lasts for a relatively shorter time than that of the lower temperature line of Fe xviii 9.39 nm, and the situation is reversed for the Type II flares. It implies that the heating process in Type II flares may be more impulsive so that the plasma can be heated to higher temperatures than in Type I flares.

A statistical analysis is done for the 52 flares, among which 24 flares belong to Type I and 28 flares to Type II. Here we use the parameter $\frac{\text{Class}}{\text{PeakTime} - \text{BeginTime}}$, which are all inferred from the *GOES* SXR emission, as a proxy of the rise rate of a flare. It is found that in the plane of the rise rate and SXR peak intensity (Figure 17(a)), the Type I flares are generally located on the left of the Type II flares, suggesting a slower heating of Type I than Type II flares. Furthermore, the cooling rates of the two types of flares are distinct too, as shown in Figure 17(b). Type I flares also tend to have a slower cooling rate or longer cooling time. We believe that this is because Type I flares heat plasma to a

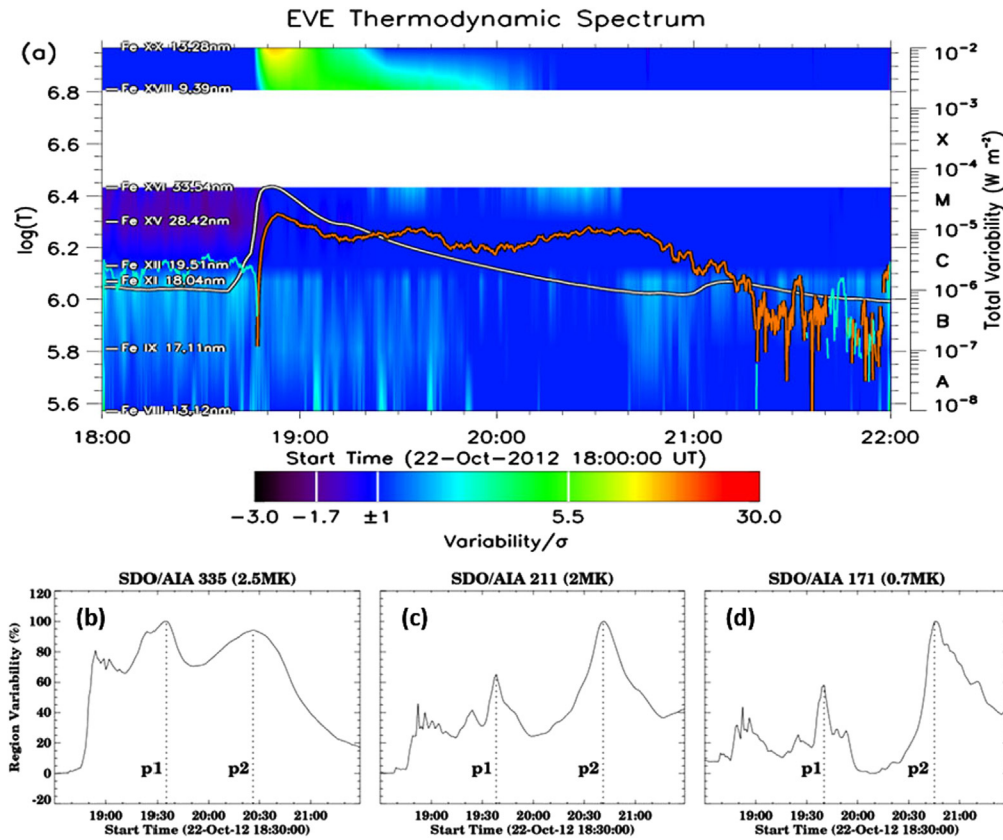


Figure 19. Triple-peak flare occurring on 2012 October 22. (a) TDS chart for the event, in which the integrated flux indicated by the orange line shows three significant peaks. (b)–(d) The light curves from the *SDO/AIA* 33.5 nm, 21.1 nm, and 17.1 nm, respectively, which are the integration over the flaring region as shown in Figure 20.

relatively lower temperature at a relatively slower rate than Type II flares, and therefore for the same amount of released energy, Type I may last longer and show a gradual behavior.

4.3. The Flares with a Late Phase

In Section 3 we mentioned the eruptiveness of the four flares. For the two flares without a late phase, the long-duration flare is eruptive, whereas the short-duration flare is confined. However, for the other two flares with the late phase, the eruptiveness is apparently not related to the duration, as one of them (case C2) is confined though it lasted for more than 5 hr. For that particular event, we noticed that it has a strong late phase, i.e., the peak of the late phase is higher than that of the main phase. On the contrary, the eruptive flare (case E2) has a weak late phase. We believe that the late phase might carry some information on the behavior of a flux rope which is trying to escape from the Sun. A strong constraint of the overlying arcades may prevent a flux rope from escaping, and cause the energy carried by the flux rope to be re-deposited into the thermal emissions which forms a stronger late phase. Case C2 fits this scenario, as suggested by Liu et al. (2015). The long-duration confined X-class flare reported by Liu et al. (2014) also had a significant late phase, as shown in their Figure 3. On the other hand, if the flux rope successfully made its way out, a smaller fraction of its energy will be consumed as thermal emissions, and a weaker late phase will form.

To check this speculation, we check all the late-phase flares in our sample of M5.0+ flares. There are 12 flares with a clear late phase, as listed in Table 4. All these events are confirmed with *SDO/AIA* images to ensure that the late-phase peak is related to the main-phase peak. The values of the late-phase peaks are read from the orange lines in the TDS charts. To make the comparison more convenient, we use “C,” “M,” and “X,” to mark the intensity of the peaks, just like the SXR class. From Table 4, one can find that there could be multiple late-phase peaks (events L1, L7, and L8) and the interval between the main-phase peak and the first late-phase peak could be as short as 33 minutes (event L6) or as long as more than 3 hr (event L12). By comparing the intensity of the first late-phase peak with that of the main-phase peak read from the TDS charts, we find a rough correlation between the TDS peak ratio, which is $\frac{\text{TDSLatePhasePeak1}}{\text{TDSMainPhasePeak}}$, and the flare class defined by the SXR main-phase peak, as shown in Figure 18. Except the events L8 and L10, the late-phase peaks of the confined flares are systematically stronger than those of the eruptive flares. Strictly speaking, the pattern in Figure 18 suggests that a flare with a stronger late phase must be confined. Although the sample is small, the result does preliminarily justify our speculation before. An analysis based on a larger sample is worthwhile.

The multiple late-phase peaks were mentioned before by Dai et al. (2013) and Liu et al. (2015). In our 12 cases, there are 3 flares with clear multiple peaks during the late phase. The intervals between these multiple peaks vary from about

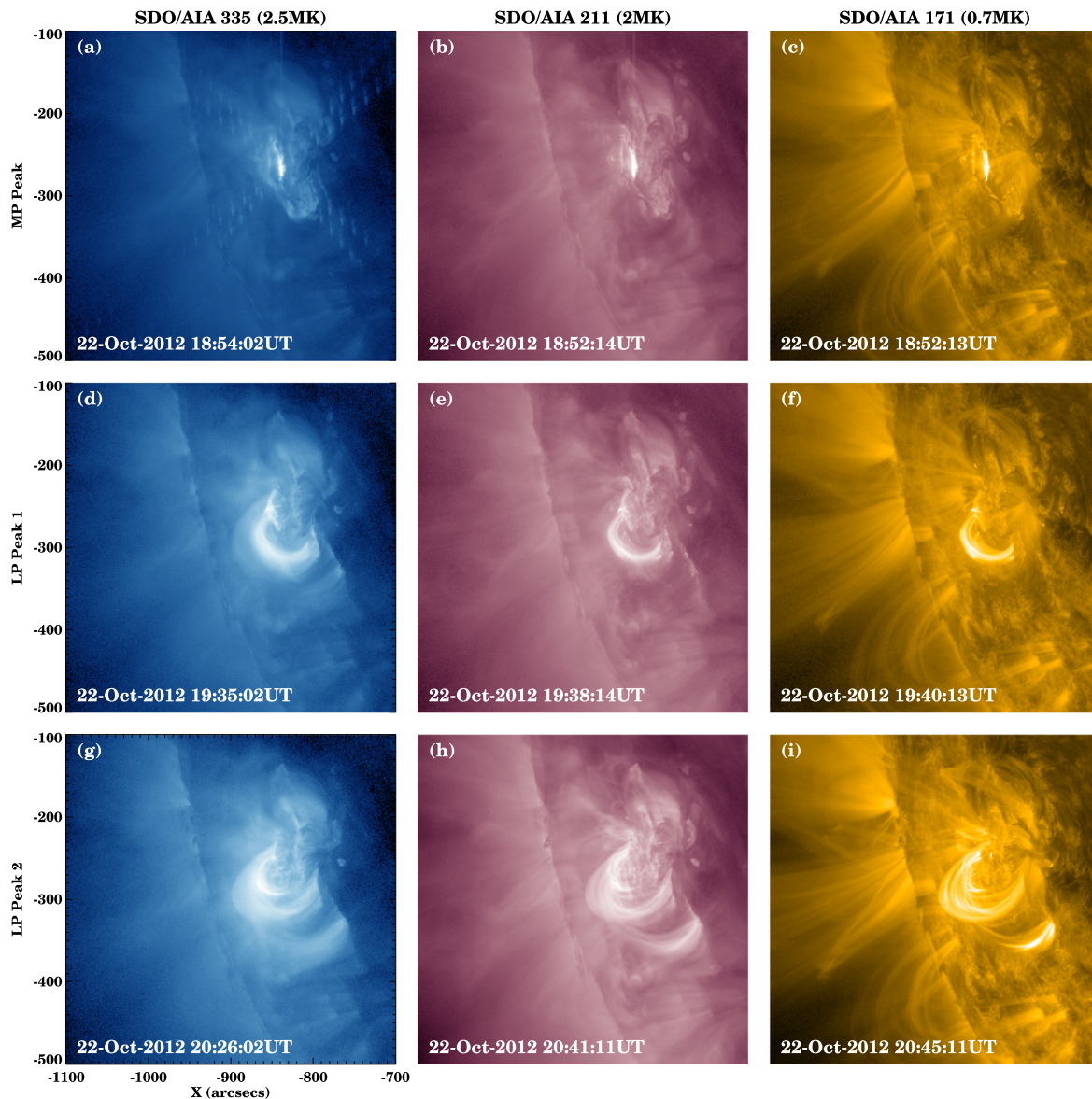


Figure 20. *SDO/AIA* images showing the flaring region of the 2012 October 22 event. From left to right, the panels are for AIA 33.5 nm, 21.1 nm, and 17.1 nm, respectively. From top to bottom, the panels display the flaring loops/arcades during the main-phase peak and the two late-phase peaks, respectively.

55 minutes to about 89 minutes. There is no obvious regulation among these multiple peaks. A flare with multiple late-phase peaks could be either eruptive or confined. Figure 19 shows a triple-peak flare on 2012 October 22 (the event L7). In panel (a), one can see one main-phase peak plus two significant late-phase peaks. Emissions from the line of Fe XVI 33.54 nm most clearly show these peaks. Similar signatures could also be found in the lines of 21.1 nm and 17.1 nm. Figure 20 displays the flaring region viewed through *SDO/AIA* 33.5 nm, 21.1 nm, and 17.1 nm, respectively, during the three peaks. The light curves from these three passbands integrated over the flaring region are presented in panels (b)–(d) of Figure 19. This confirms that these peaks came from the same event. In particular, from Figure 20, the main-phase peak originated from the lowest loops or the core field, the first late-phase peak from the higher arcades near to the core field, and the second late-phase peak from the outmost arcades.

5. EXTENDED TDS CHARTS WITH THE *SDO/EVE* MEGS-B DATA

5.1. Method

According to the flare catalog⁷ compiled by the EVE team, MEGS-B captured 82 M-class flares and 6 X-class flares though it did not operate full time. However, not all of these flares are completely covered by the MEGS-B data in time. That is why we did not use it in the statistical study of the M5.0 + flares. Here we introduce how we extend the TDS charts with the MEGS-B data, and show some examples.

There are 15 lines from MEGS-B in the EVL product, among which 8 lines, Nos. 2, 4, 9, 10, and 12–15 in Table 5, are significantly blended by other ions based on our criterion given in Section 2.1. All these contaminated lines are discarded. Further, the lines Si XII 49.94 nm and Ne VIII

⁷ http://lasp.colorado.edu/eve/data_access/evewebdata/interactive/eve_flare_catalog.html

Table 5
Emission Lines Provided by MEGS-B EVL Product*

No.	Ions	λ_{\min} (nm)	λ_{\max} (nm)	λ_{cen} (nm)	$\log(T)$ log(K)	σ_{\pm} ($\times 10^{-7} \text{ W m}^{-2}$)	$\sigma_{G\pm}$ ($\times 10^{-9} \text{ W m}^{-2} \text{ s}^{-1}$)
1	Si XII	49.84	50.04	49.94	6.29
2	Mg X	62.28	62.68	62.49	6.05
3	Ne VIII	76.90	77.18	77.04	5.81
4	Ne VII	46.32	46.74	46.52	5.71
5	O VI*	103.10	103.32	103.19	5.47	+19.2/−11.7	+5.5/−4.2
6	O V*	62.74	63.18	62.97	5.37	+8.4/−5.7	+1.7/−1.3
7	O IV*	55.20	55.64	55.44	5.19	+2.8/−1.7	+0.8/−0.6
8	O IV	78.90	79.14	79.02	5.19	+3.1/−1.9	+1.3/−1.2
9	O III	52.42	52.72	52.58	4.92
10	O III	59.84	60.14	59.96	4.92
11	C III*	97.56	97.86	97.70	4.84	+48.7/−22.0	+13.9/−9.9
12	O II	71.72	72.00	71.85	4.48
13	He I	58.22	58.68	58.43	4.16
14	H I	97.08	97.44	97.25	3.84
15	H I	102.42	102.70	102.57	3.84

Note.

* Columns 3–5 give the wavelength range and peak wavelength of each spectral line, Column 6 lists the corresponding formation temperature, and the last two columns give the deviations of the variabilities and gradients of final selected spectral lines (see Section 2.2 for more details).

77.04 nm have a formation temperature very close to the lines Fe XV 28.42 nm and Fe IX 17.11 nm, respectively, which have been used in the TDS charts. Thus, the two lines are not considered. In the remaining, line Nos. 7 and 8, i.e., O IV 55.44 nm and 79.02 nm, have the same corresponding temperature. After the testing, we find that the two lines are quite similar. The line O IV 79.02 nm is slightly more sensitive than O IV 55.44 nm (see the deviations listed in the last two columns of Table 5). A larger sensitivity sometimes means that it is easy to get noisy, and the normalization based on a larger deviation will reduce the significance of real signals. Thus, we choose O IV 55.44 nm rather than O IV 79.02 nm. Finally, four lines, which are marked by the asterisks in Table 5, are selected to construct the extended TDS charts.

The procedure of generating the extended TDS charts is exactly the same as that in Section 2.2. One can find the extended TDS charts at the webpage <http://space.usc.edu.cn/dreams/shm/tds-c09>. Figure 21 shows an example, which is the same event in Figure 2 so that one can compare them for the difference. First, it should be noted that the temperature gap between the last two lines in the TDS is large, and we do not try to interpolate the gap between them. Thus, the last line, C III 97.70 nm, is plotted separately as a stripe.

5.2. Cases

The extended TDS gives a more complete picture of the thermodynamic process of a solar flare, in which the impulsive and gradual phases of a flare (see the review by Hudson 2011) can be clearly recognized. For the particular event on 2014 January 7 (Figure 21), the enhancement of the emission started first from the temperature below $\log(T) = 5.5$, which is about two minutes ahead of the emission enhancement above the temperature of $\log(T) = 6.8$. The enhancement at the low temperature is stronger but shorter than that at the high temperature. It is due to the non-thermal heating of the accelerated electrons impacting the dense chromosphere and/or the transition region (see also, e.g., Milligan et al. 2014). This is the impulsive phase of the flare. Immediately, the impact of non-thermal particles causes the chromospheric evaporation,

which transfers the heat to the flare loops and heats them up, leading to the thermal phase during which the plasma could be observed more than 10 MK. This hot plasma then cools down in time, as can be seen from the drift pattern in either the variability chart or the gradient chart. Figure 22 shows the other two X-class flares which were completely observed by MEGS-B. Similar to the 2014 January 7 event, the emission enhancement at the low temperature in both events is slightly earlier than that at the high temperature, though the difference in time is not so significant, the strength of the enhancement at the low temperature is stronger than that at the high temperature, and the duration is relatively shorter.

The variation of the emission between $\log(T) = 5.6$ and 6.2, which is inert to enhancement but sensitive to reduction, is noteworthy. For the three X-class flares, the emission within that temperature range changed little at the beginning, but a significant reduction at a later time can be observed for two of them (as seen in Figure 21 and the lower panel of Figure 22). Both flares with the emission reduction are eruptive, and the other flare is confined. Thus, a promising explanation of such a reduction is that the accompanied CME removes a significant plasma from the corona, which is mainly located within the temperature range from about $\log(T) = 5.6$ to 6.2. A statistical survey on the CME signatures in TDS charts will be performed in a separated paper. So far, it is still a mystery why the emission corresponding to that temperature range is difficult to enhance during a flare. Whether it is simply a weakness of our TDS visualization method or if there is some unknown physical mechanism is worthy of further study.

6. SUMMARY AND DISCUSSION

In this work, we present a new method to show the thermodynamic processes of solar activities, the so-called TDS chart, which is constructed based on the *SDO*/EVE data. The TDS charts provide a global view of the thermal processes during solar flares, especially when both MEGS-A and MEGS-B data are incorporated. By investigating four flares of different types, we present in detail how to read the flare information from the TDS charts. Reading from the charts, we are able to

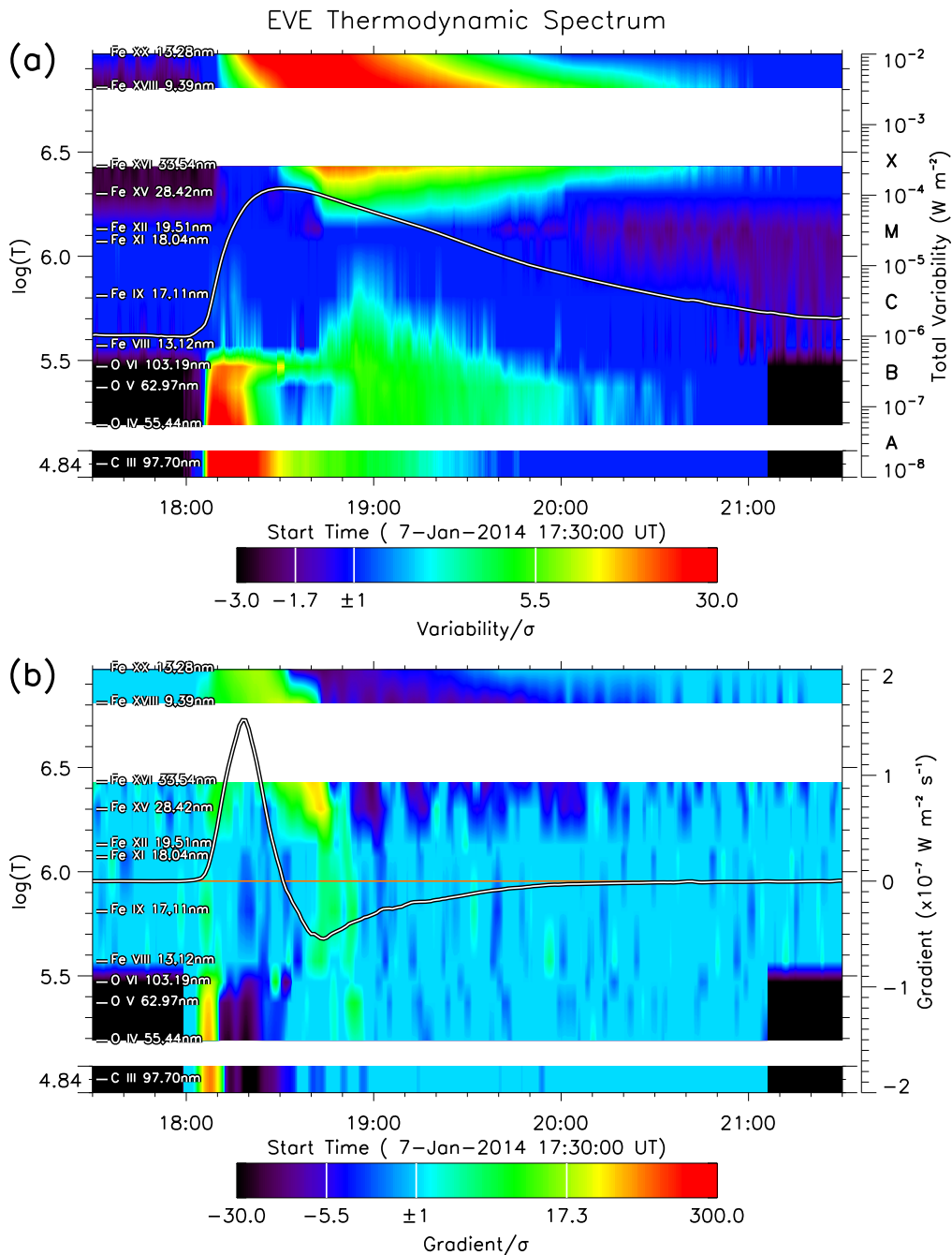


Figure 21. Extended TDS charts of the same event in Figure 2.

easily recognize if there is a late phase following a main phase of a flare, and are able to learn the start, peak, and end times of the flare as well as the drift of the temperature of the heated plasma during the flare. The advantages of TDS may not only be in studies of flares but also CMEs, and there are still some unclear signatures in TDS, as discussed in Section 5.2.

We apply the TDS method to all the M5.0+ flares during the EVE/MEGS-A's five-year lifetime. First, we measure the delay time of the EUV peaks and the cooling rates of these flares. It is found that EUV peaks are always behind the SXR peaks, and the mean value of the delay time is about five minutes. The stronger flares tend to have a faster cooling rate, and the mean value of the cooling rate is about $-0.04 MK s^{-1}$. There is a clear power-law correlation between

the cooling rates and the peak delay times, which suggests a coherent cooling process of flares within the temperature range from SXR down to EUV emissions.

Second, we find that there are two temperature drift patterns of flares in the TDS charts, called Type I and Type II. Type I flares show a quadrilateral-like drift mode from high to low temperatures with time, and the others shows a triangle-like drift mode. The statistical analysis reveals that Type I flares are generally more gradual and their heating processes are more durable than Type II flares, whereas Type II flares are impulsive and more plasma at higher temperature may be heated.

Third, the strength of the late-phase peak is relevant to the eruptiveness of a flare. A rough correlation could be found

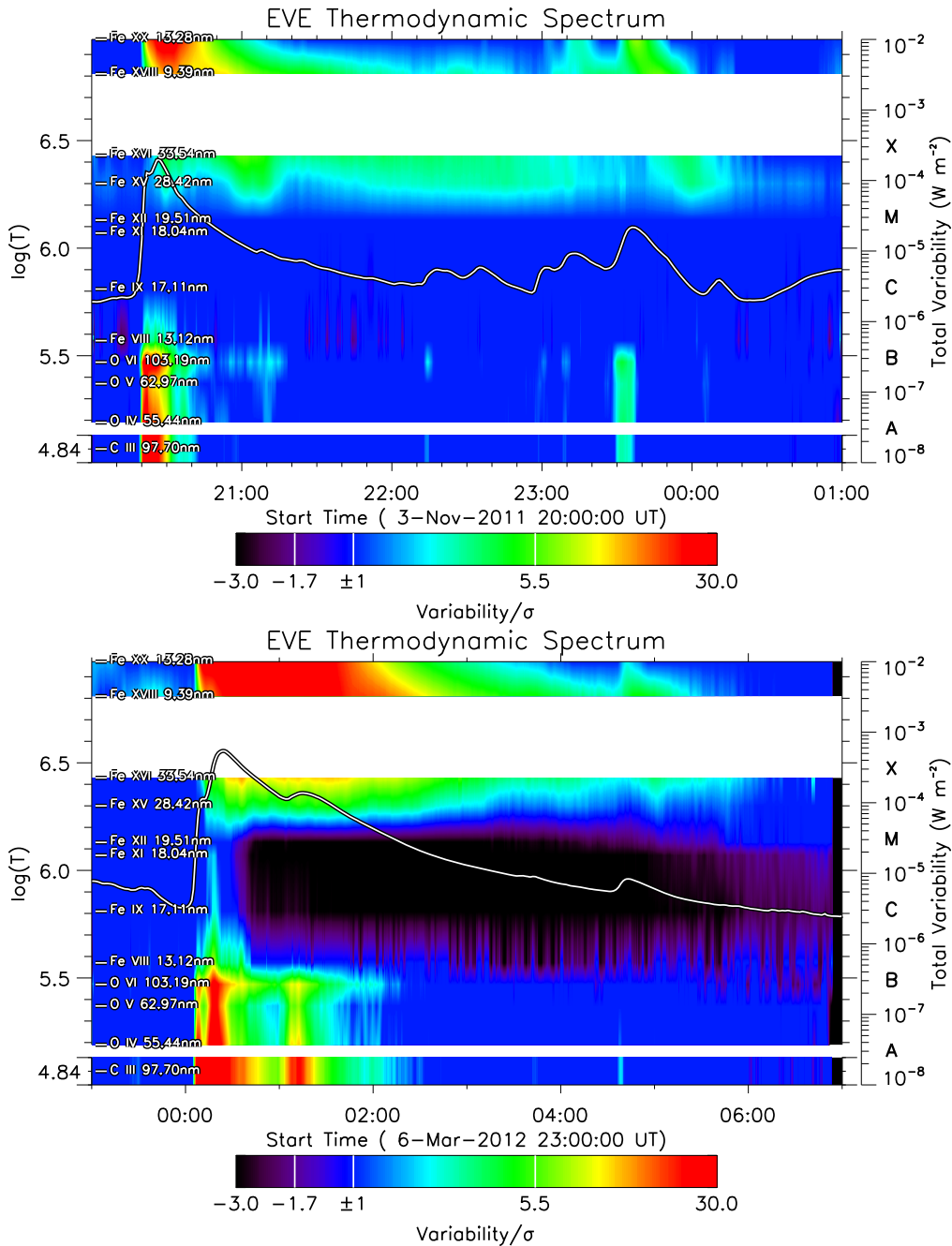


Figure 22. Two X-class flares on 2011 November 3 and 2012 March 7 shown in the extended TDS.

between the TDS peak ratio and the SXR flare class, suggesting that a strong late phase is probably caused by a confined flare, during which the energy carried by the flux rope that was trying to erupt out is re-deposited into the thermal emissions. This result gives us new clues to understand the energy partition and transfer process during the attempted flux rope eruption.

Warren et al. (2013) constructed similar charts by computing differential emission measure (DEM) distribution. Their DEM method gave the TDS within the temperature range of $\log(T) = 6.3\text{--}7.8$ without gaps. As mentioned in their paper, the weakness of such charts is that the uncertainties in DEM are difficult to assess, which is because it is model-based and many assumptions have to be made. Compared with the DEM charts, our charts are almost model-free, and the temperature range is

from $\log(T) = 5.57$ (or 4.84 if MEGS-B data are available) to 6.97. Low temperature resolution might be the weakness of our current charts, but it could be improved by incorporating more emission lines. Besides, the temperature indicated in our TDS stands for the peak formation temperature of a line, which may deviate away from the real temperature of the emitting plasma, particularly in non-isothermal circumstances. At this point, one should be cautioned about using TDS to interpret the thermal processes. However, the comparison between the TDS and DEM charts of the five events shown in Warren et al. (2013) paper (Figures 8 and 9 therein) suggests that the deviation may not be significant as their patterns look similar in the common temperature range. (One can check our online website to make the comparison.) The two kinds of charts could be complementary useful to each other.

The technique of the TDS presented here may not be only limited to solar physics. As mentioned in the introduction, since the first rocket-based experiments in 1960s, there have been many EUV observations of distant astronomical objects, e.g., stars, in the universe. Due to the far distance, there is no detailed imaging data of those stars. Thus, the TDS technique established here provides a potential approach to learn about the stellar eruptive activities.

We acknowledge use of data from the *SDO*, *STEREO*, *SOHO*, and *GOES* spacecraft. *SDO* is a mission of NASA's Living With a Star Program, *STEREO* is the third mission in NASA's Solar Terrestrial Probes program, and *SOHO* is a mission of international cooperation between ESA and NASA. The TDS charts for all the events involved in this study could be found at <http://space.ustc.edu.cn/dreams/shm/tds> (the MEGS-A-only TDS) and <http://space.ustc.edu.cn/dreams/shm/tds-c09> (the extended TDS). This work is supported by grants from the NSFC (41131065, 41574165, 41421063, 41274173, 41222031, 41404134, and 41474151), CAS (Key Research Program KZZD-EW-01 and 100-Talent Program), MOST 973 key project (2011CB811403), and the fundamental research funds for the central universities.

REFERENCES

- Brueckner, G. E., Howard, R. A., Koomen, M. J., et al. 1995, *SoPh*, 162, 357
- Chamberlin, P. C., Milligan, R. O., & Woods, T. N. 2012, *SoPh*, 279, 23
- Craig, N., Abbott, M., Finley, D., et al. 1997, *ApJS*, 113, 131
- Dai, Y., Ding, M. D., & Guo, Y. 2013, *ApJL*, 773, L21
- Dere, K. P., Landi, E., Mason, H. E., Monsignori Fossi, B. C., & Young, P. R. 1997, *A&AS*, 125, 149
- Dere, K. P., Landi, E., Young, P. R., et al. 2009, *A&A*, 498, 915
- Emslie, A. G., Dennis, B. R., Shih, A. Y., et al. 2012, *ApJ*, 759, 71
- Friedman, H. 1963, *ARA&A*, 1, 59
- Fröhlich, C., & Lean, J. 2004, *A&ARv*, 12, 273
- Harrison, R. A. 1995, *A&A*, 304, 585
- Hudson, H. S. 2011, *SSRv*, 158, 5
- Jiang, Y. W., Liu, S., Liu, W., & Petrosian, V. 2006, *ApJ*, 638, 1140
- Lemen, J. R., Title, A. M., Akin, D. J., et al. 2012, *SoPh*, 275, 17
- Liu, K., Wang, Y., Zhang, J., et al. 2015, *ApJ*, 802, 35
- Liu, K., Zhang, J., Wang, Y., & Cheng, X. 2013, *ApJ*, 768, 150
- Liu, R., Titov, V. S., Gou, T., et al. 2014, *ApJ*, 790, 8
- Liu, Y. 2008, *ApJL*, 679, L151
- Milligan, R. O., Chamberlin, P. C., Hudson, H. S., et al. 2012a, *ApJL*, 748, L14
- Milligan, R. O., Graham, S. K., Brian, R. D., et al. 2014, *ApJ*, 793, 70
- Milligan, R. O., Kennedy, M. B., Mathioudakis, M., & Keenan, F. P. 2012b, *ApJL*, 755, L16
- Moore, C. S., Chamberlin, P. C., & Hock, R. 2014, *ApJ*, 787, 32
- Pawłowski, D. J., & Ridley, A. J. 2008, *JGR*, 113, A10309
- Pesnell, W. D., Thompson, B. J., & Chamberlin, P. C. 2012, *SoPh*, 275, 3
- Qian, L., Burns, A. G., Chamberlin, P. C., & Solomon, S. C. 2010, *JGR*, 115, A09311
- Ryan, D. F., Chamberlin, P. C., Milligan, R. O., & Gallagher, P. T. 2013, *ApJ*, 778, 68
- Sutton, E. K., Forbes, J. M., Nerem, R. S., & Woods, T. N. 2006, *GeoRL*, 33, L22101
- Wang, Y., & Zhang, J. 2007, *ApJ*, 665, 1428
- Warren, H. P. 2006, *ApJ*, 637, 530
- Warren, H. P., Mariska, J. T., & Doschek, G. A. 2013, *ApJ*, 770, 116
- Woods, T. N., Kopp, G., & Chamberlin, P. C. 2006, *JGR*, 111, A10S14
- Woods, T. N., Hock, R., Eparvier, F., et al. 2011, *ApJ*, 739, 59
- Woods, T. N., Eparvier, F., Hock, R., et al. 2012, *SoPh*, 275, 115
- Yashiro, S., Akiyama, S., Gopalswamy, N., & Howard, R. A. 2006, *ApJL*, 650, L143
- Zhang, J., Cheng, X., & Ding, M.-D. 2012, *NatCo*, 3, 747